EXPERIMENTS ON TURBULENT FLOW SEPARATION

Jonas Gustavsson

Abstract

A turbulent boundary layer was subjected to adverse pressure gradients of different strengths and the effects this had on the pressure distribution, wall shear stress, mean velocity and perturbation velocity moment profiles were studied. Measurements were made using Particle Image Velocimetry (PIV) and the results of these examinations were compared to the results obtained from conventional measurements using static pressure taps, a Preston tube and a hot-wire anemometer. Three different cases were examined: 1. Complete separation, 2. Separation bubble and 3. Attached boundary layer subjected to a strong adverse pressure gradient (APG).

In the first case that was studied, the adverse pressure gradient was so strong and persistent that there was no reattachment in the studied region. This case was used to evaluate some empirical methods for the simulation of boundary layer development, based on the integral momentum equation [5], [10], which were found to predict the boundary layer growth rather well. However, all the examined methods indicated separation too far upstream in the separated case that was studied, and the method proposed by Stratford [30] also falsely indicated that there was separation in the least rapidly expanded flow studied.

In the second case where there was a limited area of reversed flow – a so-called separation bubble – PIV was used to study the flow in the reattachment region, while the separation line was kept fixed with a separation trip. It was found that the shape factor H decreased from its maximum value of around 15 to 3.1-3.4 at reattachment, which is higher than the value of H=2.85 reported by Alving and Fernholz [1], but lower than the value of 4.0 reported by Kline [15].

In case 3, a thorough examination of a non-equilibrium boundary layer subjected to a strong APG was made. It was found that while the near-wall peak in u_{rms} disappeared as the adverse pressure gradient "worked" on the boundary layer, sharp near-wall peaks developed in both the skewness and the flatness of the streamwise velocity. A good qualitative agreement with earlier examinations was generally found. In contrast to some of these examinations, a logarithmic sub-layer was found even far downstream at H=2.4. Instead of disappearing, the logarithmic region seemed to move inward – at H=2.4 it stretched from around 10 to 40 y^+. When the velocities in this region were used to calculate wall shear stresses, fair agreement with measurements using Preston tubes was found.

Apart from its appealing ability to study the 2D structure of a separated region, PIV was regrettably also found to suffer from a few drawbacks, most notably its low spatial and temporal resolution and its tendency towards giving a discrete velocity distribution.

Contents

Nomenclature

Co-ordinates

The origin was placed at the centre of front tip of the plate, see figure 2.

x: co-ordinate along the plate in the direction of the mean flow

y: the vertical distance from the plane of the plate

z: spanwise co-ordinate orthogonal to x and y, directed away from the side observation window of the wind tunnel measurement section

Variables

u, v, w: flow velocities along the x, y and z co-ordinates, respectively

U, V, W: mean flow velocities along the x, y and z co-ordinates, respectively

u', v' ,w': turbulent perturbation velocities along the x, y and z co-ordinates, respectively

u_{rms}: root mean square value of the flow velocity along the x-axis, average of $\sqrt{(u^2-U^2)}$

S: skewness of the u-velocity, average of $(u-U)^3/u_{rms}^3$

F: flatness of the u-velocity, average of $(u-U)^4/u_{rms}^4$

$U_\infty(x)$: local free-stream mean velocity the distance x from the front edge of t
he plate

$Tu \equiv u_{rms}/U$: turbulence intensity

$$y^+ = \frac{y}{\nu}\sqrt{\frac{\tau_w}{\rho}}$$: non-dimensional vertical co-ordinate

$u^+ = u/u_\tau$: non-dimensional velocity

ν: kinematic viscosity of air, $1.5 \cdot 10^{-5}\, m^2 s^{-1}$ (at present conditions, p=1 atm, T=294K)

ρ: density of air, 1.20 kgm^{-3} (at present conditions)

p: static pressure

p_t: static pressure at the throat

p_0: stagnation pressure

$q=0.5\rho u_\infty^2$: dynamic pressure

$q_0=q(0)$: dynamic pressure at the tip of the plate

q_t: dynamic pressure in the free-stream at the throat, i e at the smallest height section

τ_w: wall shear stress

$c_f=\tau/q$: friction coefficient

$c_\tau=c_f/2$: wall-shear stress coefficient

$u_\tau \equiv \sqrt{(\tau/\rho)}$: friction velocity

u_s: velocity scale for Perry-Schofield co-ordinates

κ=0.41: von Kàrmàn's constant for the log law of the turbulent boundary layer

$B=2.86\delta^* u_\infty/u_s$: boundary layer thickness for Perry-Schofield co-ordinates, but also a constant in the log-law for turbulent velocity profiles

$\Gamma=\theta/U\, dU/dx\, Re_\theta^{0.25}$: shape factor used by Buri for turbulent boundary layers

$C_p=(p-p_t)/q_t$: pressure recovery

$p^+=\nu/\rho u_\tau^3\, dp/dx$: non-dimensionalised pressure gradient

$\beta=\delta^*/\tau_w\, dp/dx$: equilibrium boundary layer parameter

m: equilibrium boundary layer parameter, $U \propto (x-x_0)^m$, where x_0 is a constant

$\prod$: Wake region parameter used in Coles' wake law

δ: any boundary layer thickness

$u(\delta_{0.99})=0.99u_\infty\ \delta_{0.99}$: 99% velocity thickness

$$\delta^* = \frac{1}{U_\infty}\int_0^\infty (U_\infty - U)dy$$: displacement thickness

$$\theta = \frac{1}{U_\infty^2}\int_0^\infty U(U_\infty - U)dy$$: momentum thickness

$$\Delta = \int_0^\infty \frac{U_\infty - U}{u_\tau}dy$$: Clauser's boundary layer thickness

$H=\delta^*/\theta$: shape factor

$K= dU/dx\, \nu/U^2$: acceleration parameter

χ: back-flow coefficient, portion of time the flow at a certain position runs against the free-stream

χ_w: back-flow coefficient closest to the plate

1. Introduction

In any viscous fluid, the no-slip condition means that the fluid adjacent to a solid surface does not move relative to the surface. The velocity of the fluid will increase gradually the further away from the surface one gets and will ultimately reach its free-stream value. The region in which this gradual increase of velocity takes place is called a boundary layer. At low Reynolds numbers (based on, for example, the distance from the front end (most up-stream position) of the solid object), the boundary layer is laminar. On a flat plate in a constant-pressure laminar flow, the velocities above the plate are described by a so-called Blasius profile, $U=U_\infty f'(\eta)$, where η is a non-dimensional parameter $\eta=y\sqrt{(U_\infty/\nu x)}$. $f(\eta)$ is the solution of the ordinary differential equation $ff''+2f'''=0$ with the boundary conditions $f(0)=0$ $f'(0)=0$, $f'(\eta\to\infty)\to1$. A Blasius profile is shown in figure 1a below. Blasius profiles have the shape factor $H=\delta^*/\theta=2.59$ for all x.

When the Reynolds number of the flow over a flat plate based on the distance from the leading edge of the plate, $Re_x=Ux/\nu$, reaches a certain value, often around $5 \cdot 10^5$, depending on e g free-stream turbulence, the coarseness of the plate and on other sources of disturbances, there is a transition from laminar to turbulent flow. Normally this transition takes place over a certain length of the plate, where minute flow disturbances develop into turbulent spots, which grow until they merge together and the whole boundary layer is made turbulent. To fix the streamwise position of transition, turbulence trips, e g wires or Dymo tapes attached to the plate, are often used. According to Schlichting [24], the Reynolds number based on the diameter of a trip wire must be at least 900 for transition to be trigged.
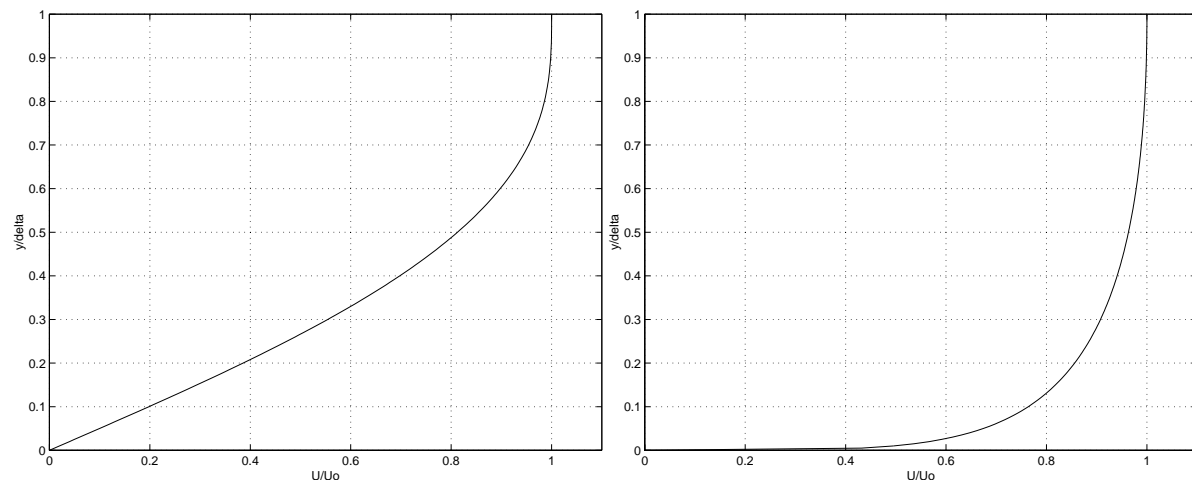

Figure 1a and b. These figures with non-dimensionalised velocity profiles show the difference between a laminar boundary layer, to the left, and a turbulent boundary layer, to the right.

After transition, the boundary layer becomes turbulent and the velocity profile changes so that the velocity gradient, $\partial u/\partial y$, close to the plate and hence the wall-shear stress, $\tau_w=\mu \partial u/\partial y$, increase as figure 1b indicates. In a turbulent boundary layer, the velocity distribution is much more complicated than in a laminar layer, see e g Rotta [21]. A non-dimensional distance from the wall $y^+\equiv y\sqrt{(\tau/\rho)}/\nu$ and a non-dimensional velocity $u^+\equiv U\sqrt{(\rho/\tau)}$ are introduced to describe the velocity profile of the inner part of the turbulent boundary layer. In a thin ($y^+<8$) region close to the plate, the so-called viscous sub-layer, the velocity increases linearly with the distance from the plate, $u^+=y^+$. Farther out is the much thicker logarithmic region ($y^+>30$), where the velocity grows with the logarithm of the distance from

the wall, $u^+=\kappa^{-1} \ln y^+ + B$. $\kappa=0.41$ is von Kàrmàn's constant and B is a constant which is often given values in the 5-6 range for a smooth plate. For a theoretical derivation of this relation is referred to Tennekes and Lumley [31]. Between the viscous sub-layer and the logarithmic region ($8<y^+<30$) there is a smoothing region, where the viscous effects that dominate in the viscous sub-layer gradually give way to the turbulent effects that dominate in the logarithmic region. For large values of y^+, the rise in u^+ gradually comes to a halt and u reaches its free-stream value. This region, which is sometimes referred to as the wake region, starts at around 0.15 δ for zero pressure gradient flows. (δ is the physical boundary layer thickness.) Notice that a self-similarity of the entire boundary layer similar to that found in a laminar Blasius boundary layer does not exist in the turbulent case. In fact, as Clauser [7] has shown, a turbulent boundary layer at zero pressure gradient when U is scaled as $(U-U_\infty)/u_\tau$ and y as y/δ, will have a shape that varies in the down-stream direction, even though the shape factor remains around H=1.3 for reasonably large Re_x.

1.1. Adverse pressure gradient

When a boundary layer is experiencing an adverse pressure gradient (APG), the pressure increase in the streamwise direction retards the flow and this effect is most pronounced for the fluid elements close to the surface. This means that the shape factor H increases from its zero pressure gradient value of around 1.3, because the displacement thickness grows faster than the momentum thickness – the velocity profiles can be said to lose 'fullness'. Another result of the retardation of the fluid closest to the surface is that the wall shear stress, τ_w, is reduced when there is an adverse pressure gradient. This means that a lower drag can be achieved and several researchers, e g Stratford [29] have studied flows that experience adverse pressure gradients large enough to make the wall shear stress minimal over a large portion of the surface. According to Schubauer and Spangenberg [25], an initially steep pressure gradient which is gradually relaxed further down-stream, will make a higher pressure recovery C_P possible over a certain distance, than a more constant pressure gradient over the same distance. Earlier, a more general examination of the behaviour of a flow under favourable and adverse pressure gradients was made by Nikuradse [18] in converging and diverging water channels. He found that not only do the boundary layers grow fast in divergent flow, but also that at a certain angle (around 5° half-angle), the flow becomes unstable and starts to fluctuate between the two sides of the channel. This instability is also discussed by Simpson [26].

When the adverse pressure gradient is strong enough, the logarithmic boundary layer representation can no longer be used. Instead, several researchers have tried to find universal profiles that can be used for decelerated boundary layers, but so far no one has managed to find a single scaling that would make profiles for all values of H fall on the same curve in a non-dimensionalised U-y-plot. Alving and Fernholz (AF) [1] have examined several different scaling techniques, and the most promising one, Perry-Schofield scaling, has been tested in this investigation. The other scaling techniques, including Yaglom's [32] half-power law, which were also examined by AF, were unsuccessful and have not been further tested in this examination. For so-called equilibrium, or self-similar, boundary layers, which were examined by Clauser [7], the equilibrium parameter $\beta \equiv \delta^*/\tau_w \, dp/dx$ is constant in the streamwise direction, such a scaling exists for high Reynolds numbers. Such a flow results when the free-stream velocity varies as $U \propto (x-x_0)^m$, where x_0 and m are constants. A direct numerical simulation of an equilibrium flow is presented by Henkes, Skote and Henningson [12] who investigates a flow similar to that used in the experiments by Skåre and Krogstad [27]. Unfortunately, such simulations of adverse pressure gradient boundary layers are

presently limited to low Reynolds numbers ($Re_\theta < 10^3$), so for higher Reynolds numbers, one has to rely on experimental data for turbulence model evaluation.

An adverse pressure gradient does not only alter the mean velocity profiles and thicken the boundary layer, the turbulence in the boundary layer, as measured by the root mean square, skewness and flatness of the perturbation velocity, changes too. For a more extended discussion on this is referred to the *Results* section of this report, where the perturbation velocity moments measured in this experiment are compared to those found in earlier experiments and numerical simulations.

1.2. Separation

Whenever there is a sudden expansion of the flow, e g following a rearward-facing step, which gives a sudden increase of the static pressure in the flow and retards the flow close to the surface dramatically, there is separation. Separation means that the slope of the velocity profile u(y) close to the surface becomes zero and this phenomenon, which gives rise to a vanishing wall shear stress at that so-called separation position, makes the boundary layer thicken considerably. Beyond this point, the mean flow close to the surface in the separated region runs *against* the free-stream direction.

If there is no adverse pressure gradient, the main flow will reattach to the surface again, so that a bounded area of back-flow, a so-called separation bubble, is formed. While the sharp edge keeps the front end of the separated region fixed, the position of the rear end, the so-called reattachment, may move up and down the surface that follows the sudden expansion. The length of the separation bubble will depend on the pressure distribution following the step – if the pressure is approximately constant or decreases in the streamwise direction, the flow will soon reattach to the surface, but if the adverse pressure gradient continues after the step, there will be a widening wake of back-flow behind it.

There may also be separation on a flat plate provided that the adverse pressure gradient is strong or persistent enough. In turbulent flow, the separation line is not stable, but moves to and forth in the streamwise and spanwise directions on the plate surface, thanks to the velocity variations over time present in such a flow. As in the case of a rearward-facing step, the flow can reattach to the wall again and create a separation bubble, if the adverse pressure gradient in the free-stream after the separation is relaxed. To describe the fluctuating nature of a separated region in turbulent flow, the so-called back-flow coefficient, χ, which is the share of the time the flow runs against the free-stream, is introduced. Even in constant-pressure boundary layer flow, the back-flow parameter may be non-zero in a thin layer close to the plate, according to Spalart and Coleman [28], and the amount of back-flow increases as the adverse pressure gradient gets steeper. The separated region in turbulent flows may be defined as the volume where the flow more often runs against than along the free-stream, i e where the back-flow coefficient $\chi > 0.5$.

According to Simpson [26], the simultaneous appearance of vanishing wall shear stress and the abrupt expansion of the boundary layer (or breakaway) is a feature only of a steady two-dimensional flow. In unsteady two-dimensional flow and in three-dimensional flow, one of the indications of separation may occur unaccompanied by the other. Simpson has chosen to connect separation with the breakaway, where the rotational flow region close to the wall expands abruptly, because this is what causes the detrimental effects of separation in most applications. Since two-dimensional flow with a steady free-stream velocity is the issue of this report, that distinction is not important here.

While adverse pressure gradients reduce the wall shear stress through decreasing the flow velocity close to the surface, separation is often associated with a large increase in drag because of the reduction in pressure recovery it causes. This is because the separated region means that the effective expansion of the flow is less than the geometry would indicate. On airfoils, separation therefore results in a dramatically reduced lift, so-called stall. The static pressure first decreases as the fluid accelerates around the front part of the body and then rises back to its original value at the rear end. If the rear end of the body is not slender enough, the fluid separates somewhere during the pressure rise phase. The pressure in the separated region tends to remain almost constant and this creates a 'suction' force that increases the drag of the body. The dramatic reduction in the performance of many vehicles and flow machines when there is separation is the reason for so much effort being devoted towards understanding, predicting and avoiding separation while still achieving as high a pressure recovery as possible.

The influence of free-stream turbulence

If the free-stream contains a substantial amount of turbulence, the wall shear stress increases and separation is delayed. The increased mixing also makes separation bubbles shorter through a stronger damping of the reversed flow. According to Hoffman and Gonzalez [13], the performance of diffusers can be greatly enhanced by the introduction of a few percent of free-stream turbulence, because the flow becomes more symmetrical, being attached to both sides of the diffuser, instead of undergoing the pulsating separation (see Nikuradse [18]). Hoffmann and Gonzalez increased the pressure recovery of a diffuser with the total opening angle of 20° from 58% to 71% when they introduced bars that gave 3.5% of anisotropic turbulence in the entry section of the diffuser. The price one pays for this approach is that the introduced turbulence-generating rods give a pressure loss. In their case, the loss was, however, only about 1.1% of the dynamic pressure of the free-stream, which is much less than the pressure gained.

Control

Several methods to control, that is delay in most cases, separation have been proposed. One way is simply to alleviate the adverse pressure gradient through introducing wing profiles outside the boundary layer that have a positive angle of attack which redirect the fluid towards the plate, increasing the velocity there and reducing any tendencies towards separation. Another method, which is used in this experiment to keep the flow from separating on the upper wall, is to remove the boundary layer through suction. To increase the mixing in the boundary layer and thereby the wall-shear stress and the velocities close to the plate, one can roughen the wall. There are also a number of schemes that attempt to increase the mixing in the boundary layer with so-called vortex generators. A vortex generator is a fixed mechanical device, often shaped like a wedge and about as high as the boundary layer is thick, which generates vortices that stretch down the plate behind the generator. These devices come with a price in the form of increased drag though, so they have to be carefully designed to give a positive net effect. For more information about vortex generators, see Schubauer and Spangenberg [25], who investigated a large number of different vortex generators or Rao and Kariya [20], who have investigated so-called submerged devices. These have a smaller height compared to the boundary layer thickness, which results in a smaller drag penalty than conventional vortex generators. Apart from these passive methods, there are also active control methods, where the flow is being continually examined and then modified by different mechanical actuators, or loudspeakers to counter any separation tendencies. The problem with the active approach is that large numbers of

sensors and actuators, connected to a massive computing system are probably needed in cases of engineering interest where the boundary layer is turbulent. Laminar separation seems much easier to prevent in this respect.

1.3. Motivation for this survey

There were several reasons for initiating this study of turbulent boundary layer separation. Firstly, this is a pilot study of the phenomenon, which should indicate what equipment and geometries that yield the most interesting and reliable results. Later, a more thorough examination of turbulent boundary layer separation is planned to be carried out in a wind tunnel with a larger test section. Secondly, the usefulness of PIV compared to traditional measurement methods in a separated flow was to be examined. Ultimately, the purpose will be to collect detailed data on the flow field in a separated boundary layer, which can be used to validate CFD models for separating flows.
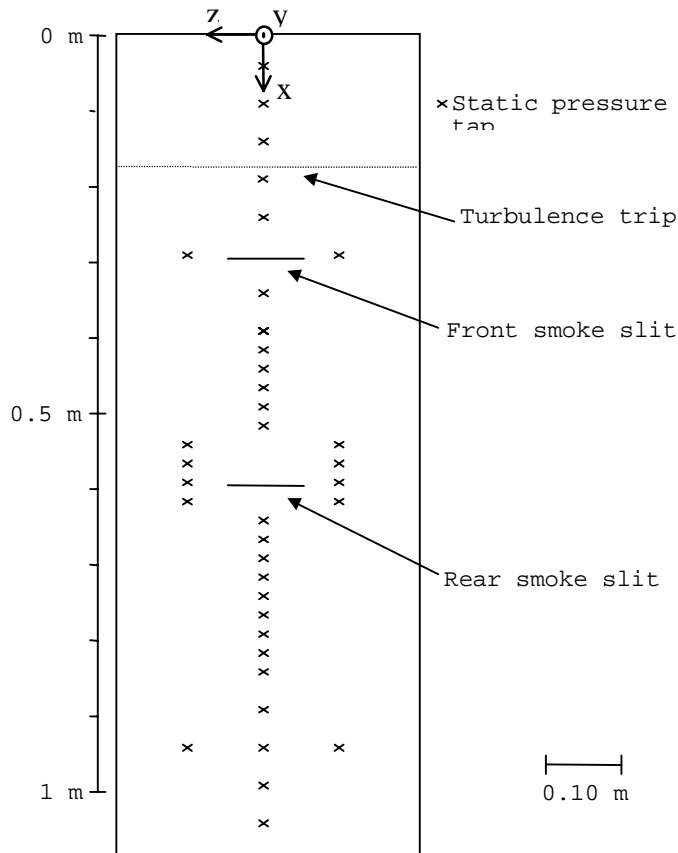
2. Experimental Set-up

Figure 2. The plexiglass plate viewed from above.

This experimental survey was carried out in one of the low velocity wind tunnels at the department. The tunnel has a measurement section with a cross-section of 0.5×0.4 m and a length of 1.15 m. The boundary layer was established on a 1.08×0.4 m large, 10 mm thick plexiglass plate which was mounted on 4 threaded rods. The lower side of the front edge of the plate was tapered at an angle of 15°. Above the plate was a bump made of 1-mm polycarbonate (Makrolon™) which was fixed to the wind tunnel ceiling in the up- and down-stream ends of the measurement section. The mid-section of the bump could be adjusted using 8 pairs of threaded rods so that different pressure distributions could be established above the plate - see figure 3. 37 static pressure holes (0.5 mm in diameter) were drilled in the plate and connected to a multi-manometer for a quick check of the pressure distribution. Most measurements were made close to the centre-line of the plate around z=-0.02 m. Some measurements were also made further away from the centre-line, to check the two-dimensionality of the flow.

2.1 Apparatus and set-up

Turbulence trip

In order to have a well-developed turbulent boundary layer at the throat, where the distance between the plate and the bump had a minimum, a turbulence trip was placed some distance up-stream. The Reynolds number of the boundary layer must be high enough at the trip, if turbulence is to be sustainable at all. After the trip, the flow was strongly accelerated, which tends to dampen turbulence. In order to achieve a boundary layer as thick as possible, to facilitate precise measurements, with as good turbulence at possible, some simple calculations and tests were made. The acceleration parameter K was calculated using the static pressure profiles for the different cases and then compared to the criterion for re-laminarisation, $K>3\cdot10^{-6}$, which was found in [16]. To check whether the trip was large enough, Schlichting's [24] criterion, that the Reynolds number based on the height of a trip wire must be at least 900 if turbulence is to be tripped, was used. It was assumed that the trip-wire diameter in Schlichting's formula could be replaced with the maximum thickness of the Dymo tape that was used as turbulence trip in this experiment. Note that a trip chosen according to this criterion is "fully efficient" according to Schlichting, but that it may

actually take some distance down-stream of the trip before the turbulence is fully developed. It was found that the x=0.18 m position constituted a good compromise for trip placement.

<u>Smoke slits</u>

Smoke could be inserted through slits 0.5 and 0.8 mm wide at the x-positions 0.3 and 0.6 m, respectively. Below the slits could be placed a mobile smoke collecting box to give a uniform smoke injection over the span of the slit. In figure 3, the smoke box is seen below the plate, mounted in its rear position. Most measurements were made with the smoke box in the upstream position to minimise disturbances in the boundary layer.

<u>Tufts</u>

A number of short tufts were taped to both the plate and the flexible bump to indicate the character of the flow, i e whether it was separated or not, at different positions. They also gave an indication of the spanwise uniformity of the flow.
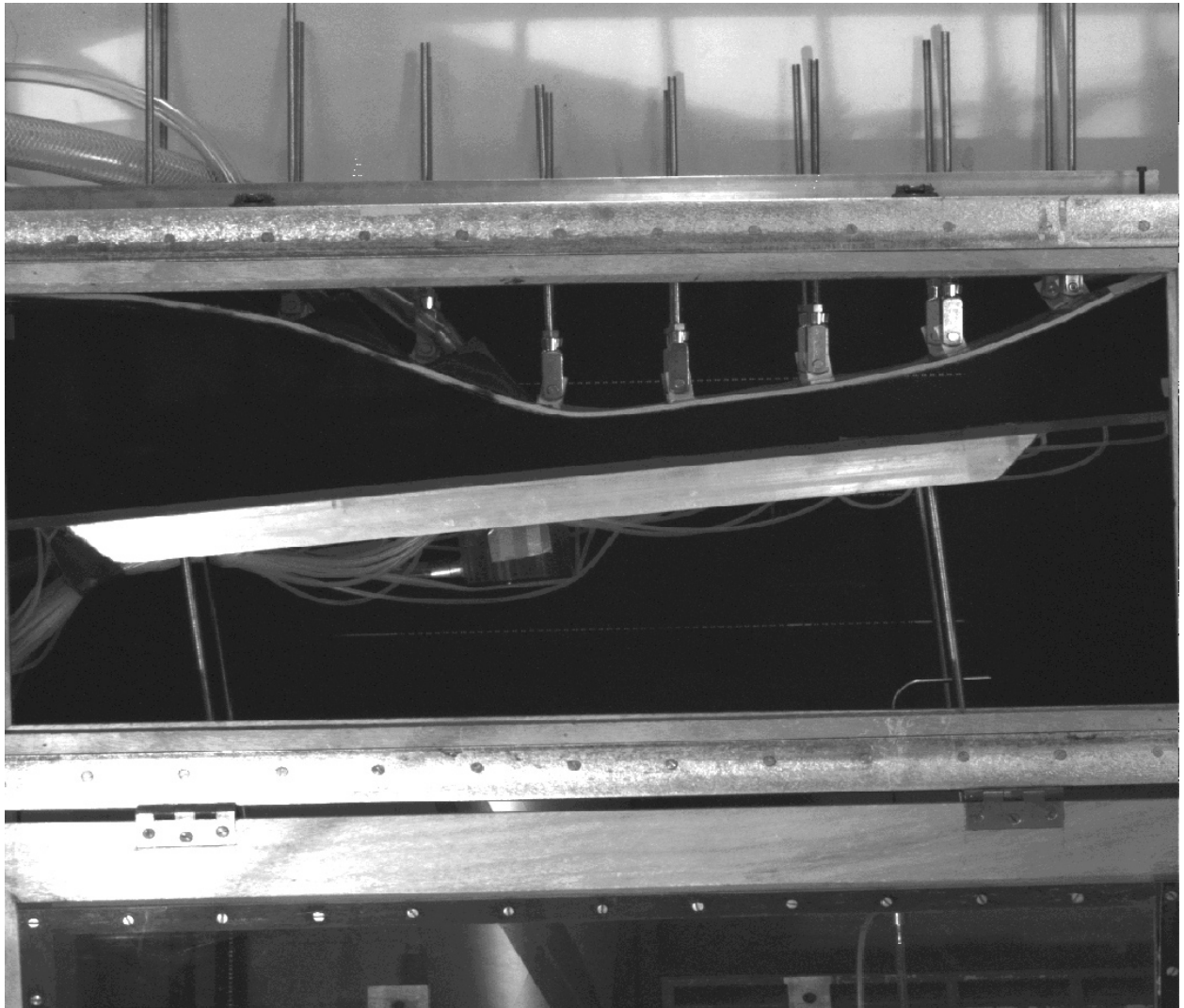

Figure 3. The measurement section with the bump and plate in their case 1a configuration. The flow is from the right to the left in the figure.

<u>Suction</u>

To make sure that there was no separation on the bump, air was being removed through 300 3 mm diameter holes drilled through the polycarbonate sheet from around the lowest point of

the bump and some 0.3 m down-stream of that position. The amount of flow that had to be removed from the upper plate was estimated as $U_\infty \delta^*$, computed at the throat, where δ^* refers to the ceiling boundary layer. To estimate these quantities, momentum integral methods were used (see section 6).

The suction system consisted of three separate suction boxes made of steel and rubber sheets as seen in the upper left corner of the measurement section window on top of the polycarbonate sheet in figure 3. They were connected to a common damping chamber with three 15-mm inner diameter PVC tubes each. The suction was established by two fans (0.75 and 0.42 kW) in series connected to the damping chamber, which gave a pressure drop of 1300 and 900 Pa over the polycarbonate plate in the first and second suction boxes, respectively. The third box, which was situated in the most down-stream position, was not used in the final set-up, since it turned out to be more efficient to concentrate the suction to the beginning of the APG region. A Prandtl tube was used to measure the flow velocity at the fan exhaust and the flow removed was estimated at 170 m^3/h, or 0.057 kg/s, which corresponds to in the order of 10% of the total flow above the plate.

Geometry

Three different ceiling configurations were used to give the four pressure distributions that were studied in the present experiment. The height profiles, i e the distance between the flat plate and the ceiling at different x-positions, are shown in figure 4 below.
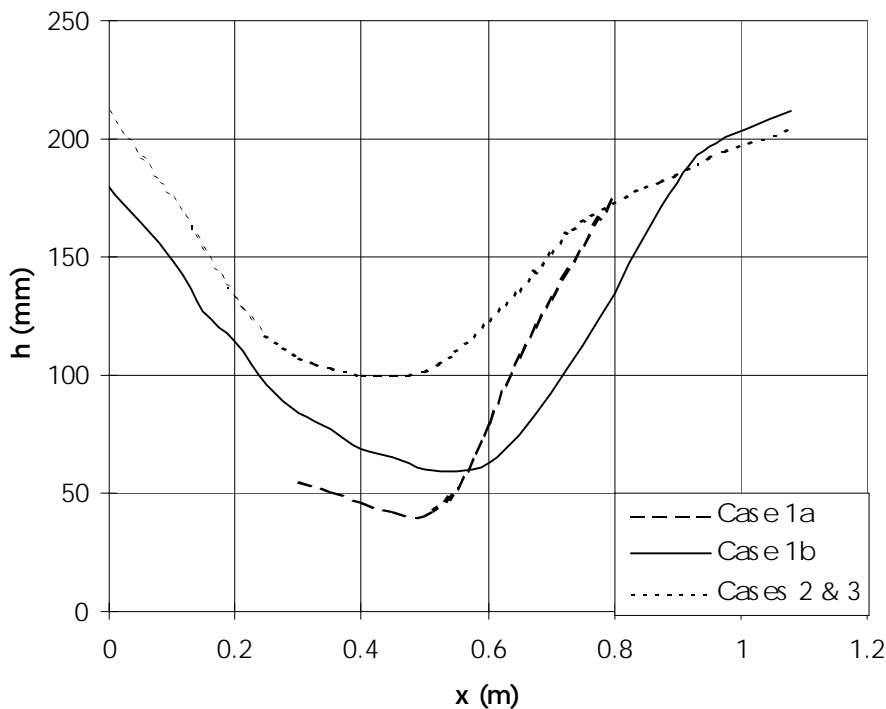

Figure 4. The height distributions of the four cases presented in this report.

2.2. Measurement techniques

A number of different measurement techniques were used to acquire pressure distributions, wall shear stresses and flow velocities over the plate.

Static pressure taps

The static pressure holes that were drilled in the plate at different x- and z-positions were connected to an alcohol-filled multi-manometer, which offered a quick check on the pressure distribution on the plate. The multi-manometer had 36 tubes and was aligned so that a resolution of about 4 Pa/mm was established. A separate electric manometer could also be used to make more precise measurements of the pressure differences between e g different static pressure taps, the stagnation pressure of the tunnel and the pressure measured with Pitot or Preston tubes.

Preston tubes

Preston tubes are Pitot tubes with a flat front end that are mounted directly on the surface facing the flow. They are used for determining the wall shear stress at their front end. A rake with 4 Preston tubes of different lengths, each 0.8 mm in outer and 0.5 mm in inner diameter that could be taped to the plate was manufactured. The rake was held together by a 2 cm wide aluminium strip, which made an angle of ca 10° with the plate to press the tubes against it. Because of the disturbance of the local flowfield the mount produced, only the most up-stream Preston tube was used. For more information on Preston tubes, see Chue [6], who gives criteria for valid use of the Preston tubes, and Bertlerud [4], who among other things describes the effects the Preston tubes have on the flowfield. The wall shear stress was calculated using Bertlerud's formula:

$$\tau_w = \frac{\Delta p}{38.85 \log_{10} \frac{\Delta p D^2}{\rho \upsilon^2} - 111.92}$$ (1)

Δp is the difference between the pressures measured by the Preston tube and a static pressure tap at the same x-position.

Hot-wire anemometry

A hot-wire mount for boundary layer measurements, consisting of a vertical traversing system in a 12 mm high, 10 mm wide aluminium bar, fixed to an aluminium plate (248 x 96 x 2 mm), which could be taped to the plexiglass plate, was used. Because the hot-wire could only be traversed to about 9 mm distance from the plexiglass plate with this mount, an extra aluminium bar to be placed between the traversing mount and the plate was manufactured. With this in place, the boundary layer out to y=19 mm could be examined. The hot-wire signal was taken from the DISA 55M01 anemometer to a MacADIOS unit and then analysed on a Macintosh computer, using a FORTRAN program to compute mean velocities and u_{rms}, as well as the skewness and flatness of the flow. The hot-wire was a 5 μm Pt wire used with 70% overheat. To get accurate data in the highly turbulent flow, about seven series, each consisting of 16384 samples taken at a frequency of 1440 Hz, were taken for each measurement point were taken. The hot-wire was calibrated against a Prandtl tube in the free-stream near the front end of the plate. The calibration was made in the range 2-40 m/s, 2 m/s being the lowest velocity at which the wind tunnel could be operated.
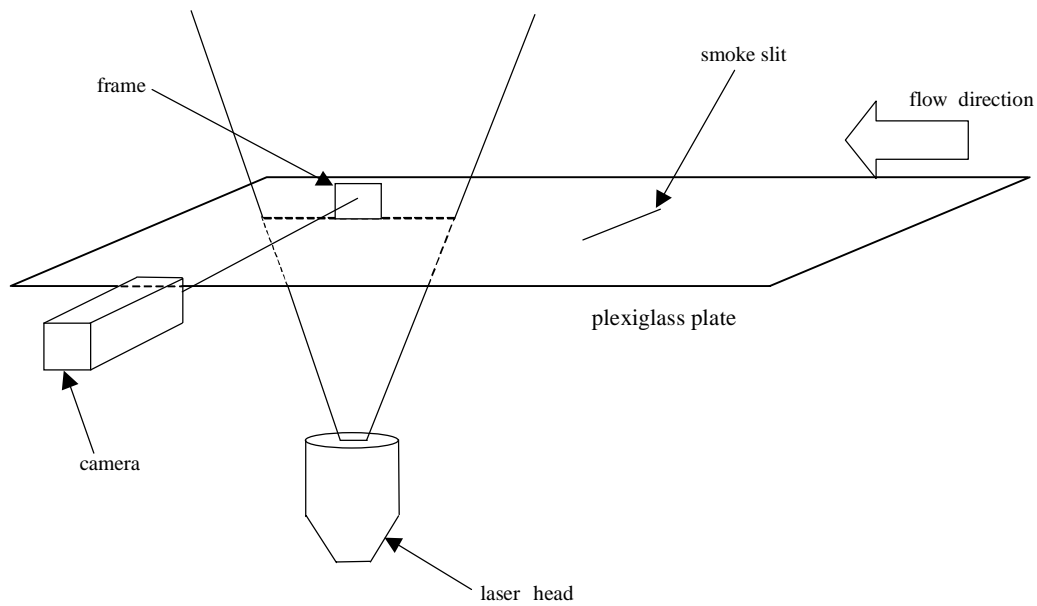
Figure 5. PIV setup.

Particle Image Velocimetry (PIV)

PIV measurements were made in a set-up with Kodak's Megaplus ES 1.0 camera, Spectra-Physics' 400 mJ PIV Nd-YAG laser, Dantec's PIV 2000 Flowmap and Flowmanager system, run on a Compaq PC. Smoke was inserted through the slit at x=0.60 m in case 1b and through both the x=0.30 m and the x=0.60 m slits in case 2 and 3. The laser-light sheet was introduced through a plexiglass window in the test section floor and the plexiglass plate and it was aligned so that the sheet was perpendicular to the z-axis at approximately z=-0.02 m to avoid interference from the static pressure taps and tubes. The camera was placed in front of the test section front window and aligned with the plexiglass plate. The field of view of the camera in the measurement plane (an xy-plane) was approximately 40x40 mm. The interrogation areas, over which average velocities are computed, were typically chosen to be 64x64 pixels with 75% overlap, which gave an apparent resolution of 0.65 mm in both the x- and the y-directions.

3. Results

Using the three different geometries presented above, three different flow cases could be studied - case 3 where an adverse pressure gradient boundary layer remained attached in the entire studied region, case 2 where it was separated for a limited distance of the plate and then reattached to it, and finally case 1 where the flow separated completely and formed a wake that extended through the entire studied region. The geometry of case 2 was the same as in case 3, but a 7 mm separation trip was introduced at x=0.67 m in the latter case. Case 1a and 1b represent different geometries, where the flow was more strongly decelerated in case 1a than in case 1b. In case 1a, where no separation trip was used, the separation line moves up- and down-stream over the plate and this smears out the average static pressures in the area of intermittent separation, making it difficult to find the exact location of mean separation. In case 1b a 10 mm wide and 3.5 mm high trip was placed at x=0.675 m to give a stable separation.

Despite the fact that the cases 2 and 3 have the same geometry and only differ in the respect that a separation trip has been introduced in case 2, the flow fields in the two cases are completely different. In case 2, a separated region is formed behind the trip in case 2, while the flow remains attached in case 3. Apart from the expected reduction of pressure recovery in the separated case, which is evident in figure 6, the static pressure distribution also indicates that the pressure recovery in the tripped case is actually much faster in front of the trip than it is in the same area when no trip is used, as is also shown in the figure. One explanation for this might be that when a separation is not tripped on the plate, there may instead be a separated region in the ceiling. If this is the case, the real expansion of the flow will be less rapid than indicated by the geometrical shape of the duct. A strong reduction in pressure gradient over the separated region as measured at the wall, due to the increased boundary-layer blockage produced by the separation, was also found in the simulation of Na and Moin [17].
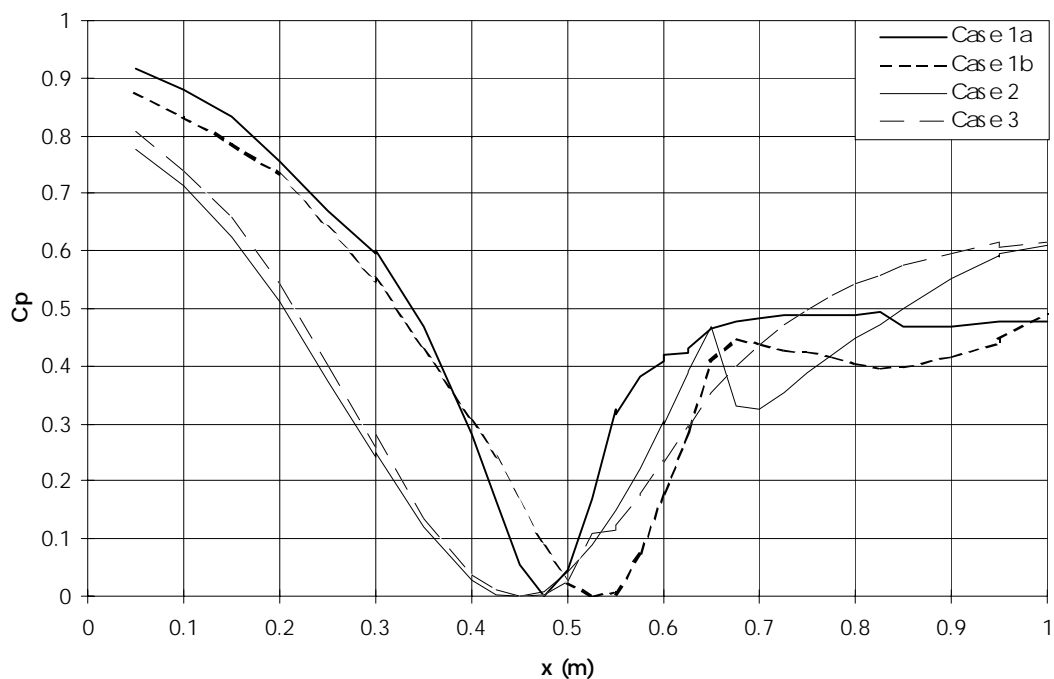

Figure 6. This is the pressure recovery in the four different cases that have been studied. Note the dip in C_P after the trips in the different cases.

Plate adjustment

To achieve a smooth leading-edge flow, the plate had to be correctly aligned relative to the on-coming free-stream. Since the ceiling near the front end of the plate consisted of the curved front fixation of the bump, the plate could not be mounted horizontally. To study the leading-edge flow, the hot-wire mount was placed close to the leading edge and a velocity profile was obtained by traversing in the y-direction.
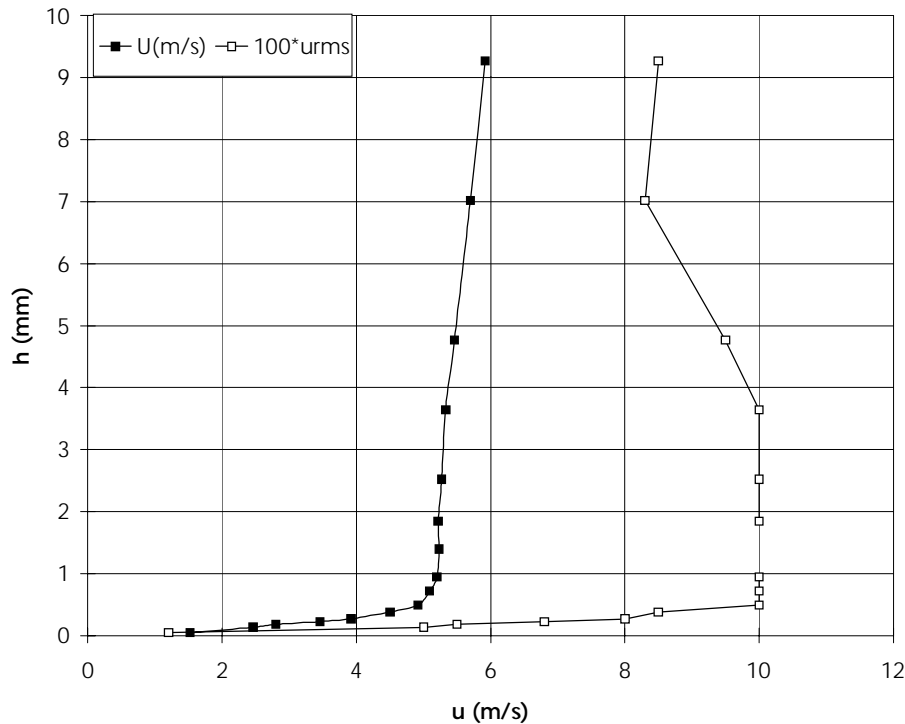

Figure 7. This figure shows the mean and perturbation velocity profiles at x=0.008 m in case 1a at low fan speed.

A velocity profile just 8 mm down-stream of the front edge of the plate at a low fan speed is shown in figure 7 above. The fact that the free-stream velocity varies in the y-direction indicates that the free-stream has not yet aligned itself with the plate, but the thin laminar boundary layer indicates that the flow is well attached to the plate near the front edge in this case.

Free-stream turbulence

The level of free-stream turbulence, u_{rms}/U, was measured using a hot-wire probe at a number of positions. Even a few centimetres ahead of the front edge of the plate, it was found to be 0.5 % and just behind the front edge (x=0.008 and 0.015 m) it had risen to 1-2%. For higher x-values, the free-stream turbulence level depends on the flow case being studied; in case 1b it was almost 2% already at x=0.35 m, while it was just 1.1% at x=0.70 m in case 3. The reason for this variation in the free-stream turbulence level was not well understood.

3.1. Completely separated flow

Preston tube measurements presented in figure 8 below show four different Preston tube pressure profiles, obtained in case 1a with different free-stream velocities. The pressure difference between the Preston tubes and static pressure taps at each position were converted to wall shear stresses using Bertlerud's conversion formula [4].

It is evident that the flow in the MR=2.5 case is qualitatively different from that at all three higher wind tunnel speeds. The three high-velocity cases have the same shape of the pressure distribution but scaled with the dynamic pressure, all indicating separation close to x=0.65 m. In the MR=2.5 case on the other hand, there seems to be separation as early as at x=0.525 m. This probably means that the boundary layer was laminar at the throat for the MR=2.5 case and hence much more sensitive to an adverse pressure gradient than the turbulent layers of higher speeds.
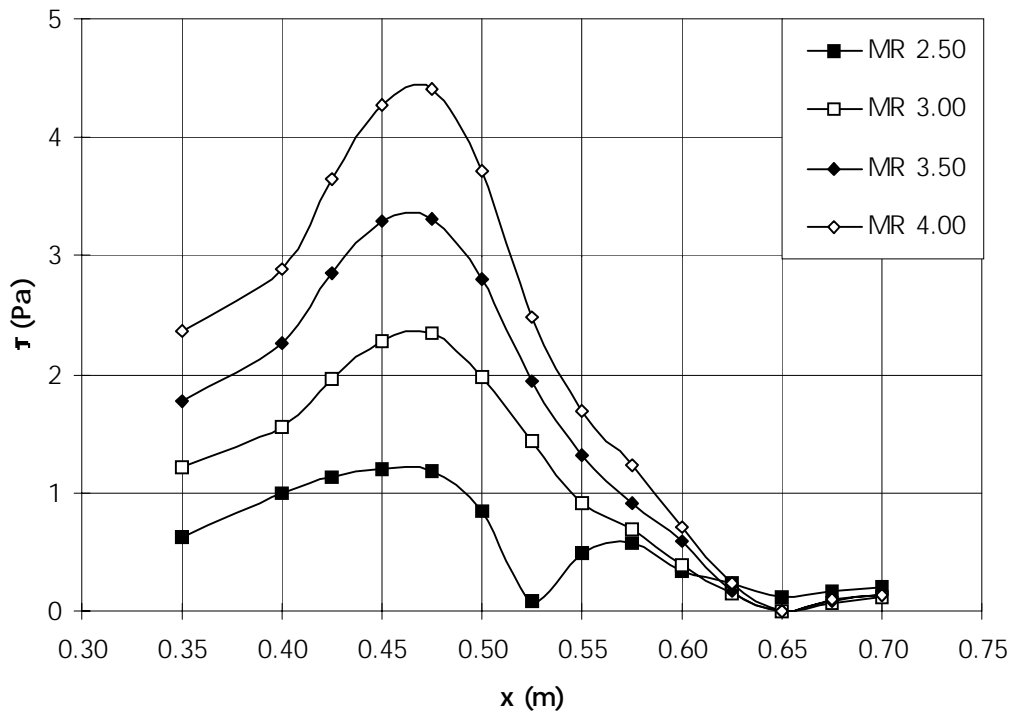
Figure 8. Wall shear stress as measured with Preston tubes in case 1a. The MR values refer to different speeds of the wind tunnel fan.

As figure 6 indicates, the pressure recovery of case 1b is similar to that of case 1a, except for the fact that there is a slight favourable pressure gradient following the trip in case 1b. This is probably due to the stable line of separation in case 1b with the near-wall flow constantly moving against the free-stream just after the trip.
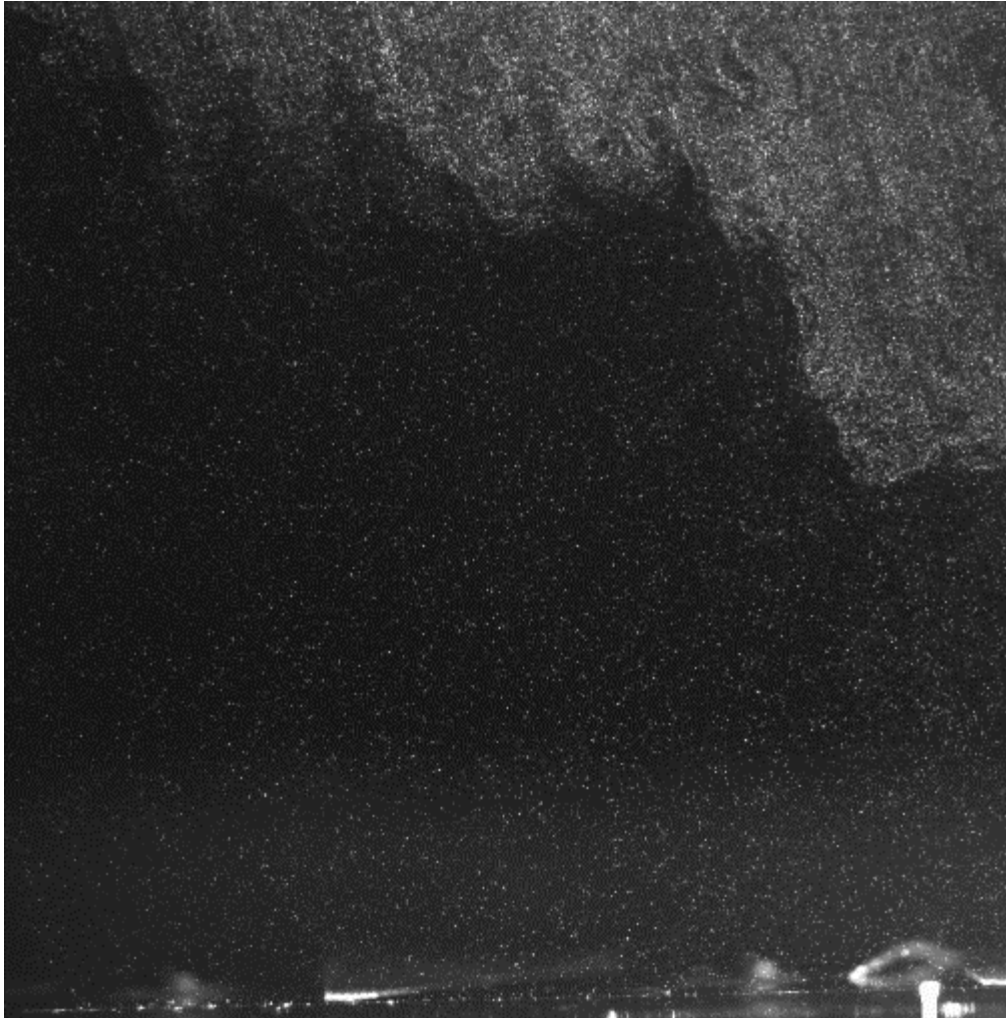
Figure 9. PIV-picture showing particles in the case 1b flow, x=0.743 - 0.783 mm. The main flow is from the right to the left in the figure. Free-stream flow direction: ⇐

In figure 9 is presented a sample PIV picture taken in case 1b down-stream of the trip, which is located 7 cm to the right of the right edge of the picture above. The positive x-direction is from right to left in the picture. It is clearly seen how the particle density is much higher in the boundary layer that separates and takes the smoke particles it contains with it, than in the reversed-flow region. Using pictures like this, instantaneous velocity fields are computed for each picture pair by the software. A coarse validation, where the least reliable velocity vectors are removed, is also performed. The instantaneous velocity field remaining after that validation is shown in figure 10. In this flow field, which corresponds to the above picture, the main flow direction is to the left as is seen in the large flow vectors in the upper part of the picture. The complex structure of the turbulent back-flow region is evident in the central and lower parts of the picture, which are full of vortices of different sizes. As is evident near the lower end of the flow field, which corresponds to the plate as captured in the picture above, the validation does not succeed in removing the apparent flow vectors that are produced by reflections in the plate surface, so these have to be removed using more refined methods.
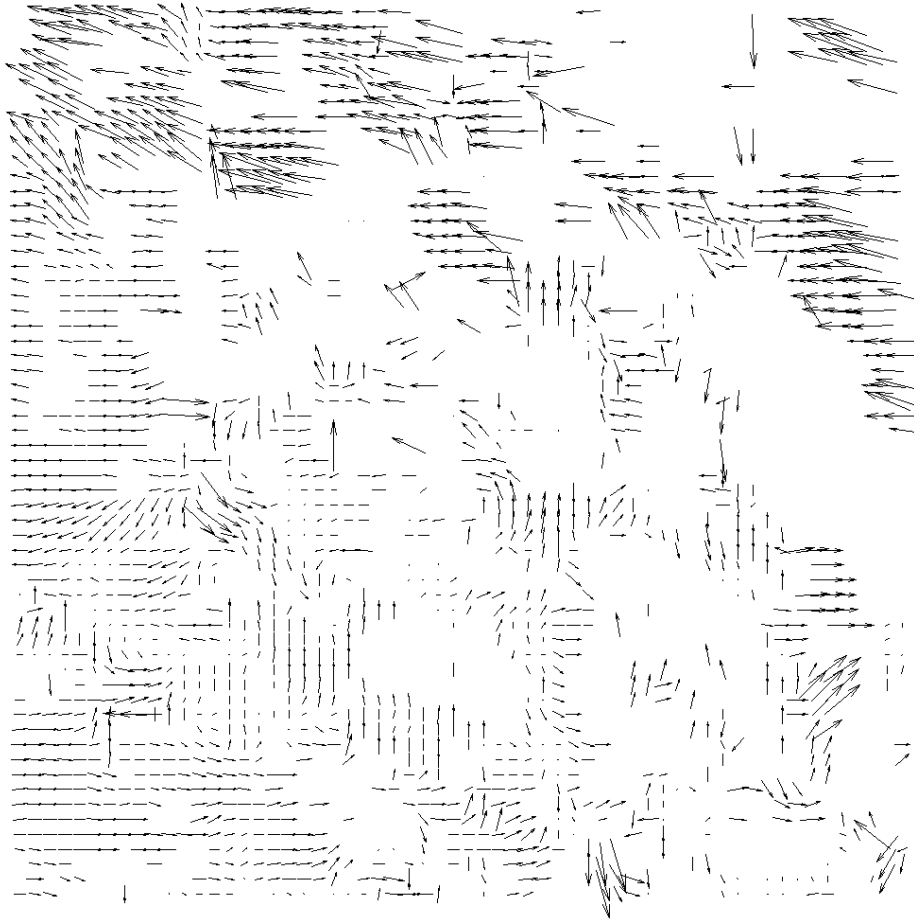
Figure 10. Instantaneous velocity field calculated from a picture pair acquired in the same area as the picture in figure 9. The displayed vectors are those that remain after the first validation. Free-stream flow direction: ⇐

To make the flowfield clearer, the resolution of the displayed vector fields in figure 11 is just one third in the vertical and one eighth in the horizontal direction of those actually acquired. It is evident from the erratic calculated mean flow vectors that the relatively small number of samples is not large enough to give accurate mean flow velocities, even when the velocities are averaged over as large surfaces as here. Figure 11 shows averages of validated flow fields, revealing a large area of back-flow. The height of the back-flow volume seemed to increase approximately linearly and 50 mm down-stream of the rear end of the trip, the height was about 30 mm. The maximum mean velocity found in the back-flow was about 6 m/s, while the free-stream velocity a couple of centimetres down-stream of the trip was approximately 25 m/s. No reattachment was found in this case, at least not in the region that could be covered by PIV measurements. Judging from the rapid growth of the reversed-flow region in that area, a reattachment further down-stream before the end of the plate seems unlikely.

After a statistical evaluation of the instantaneous velocity fields, the back-flow coefficient, χ, is calculated. The result is shown in figure 12.
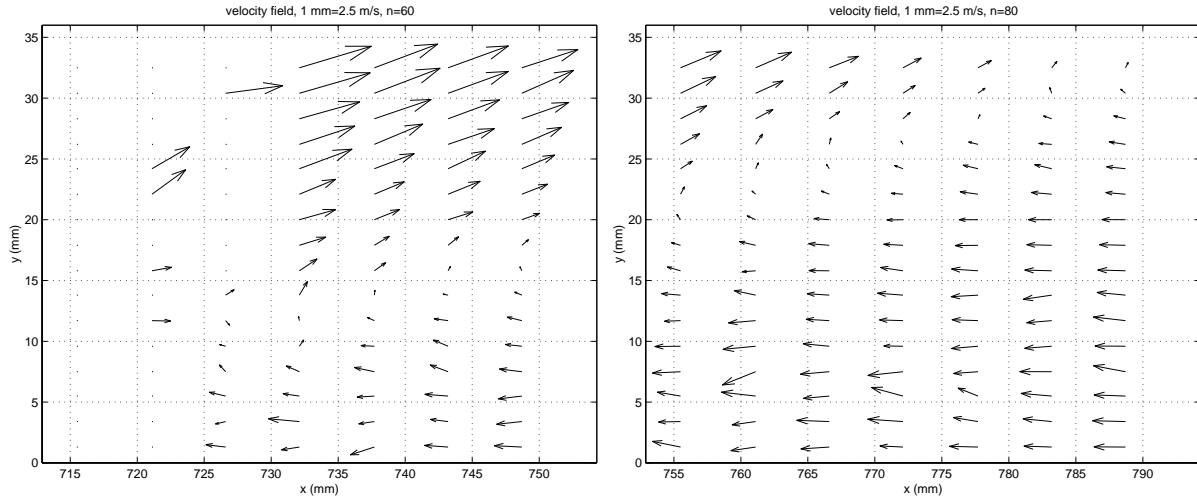
Figure 11a and b. This is the average flow field some distance down-stream of the trip. Free-stream flow direction: ⇒
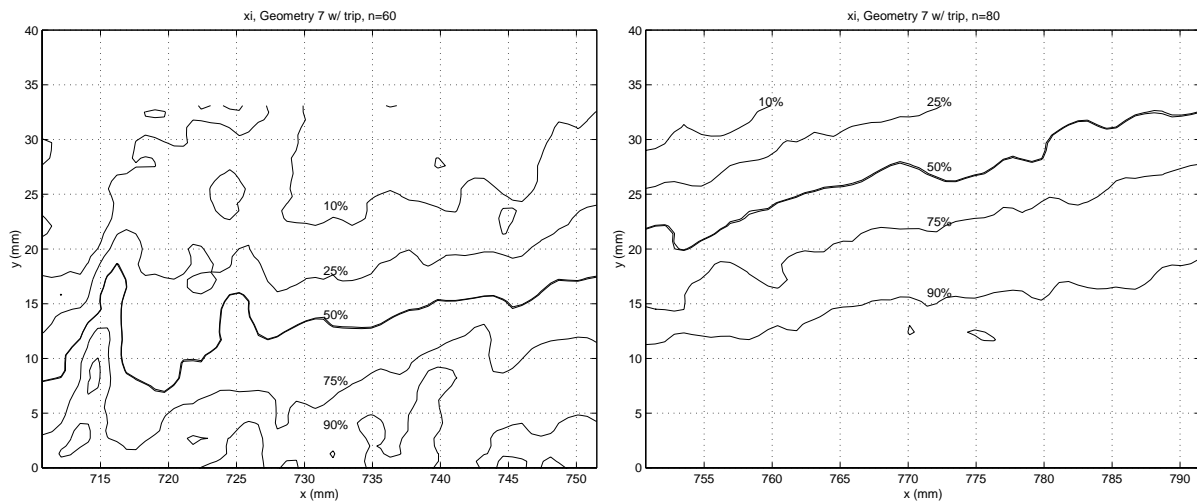

Figure 12a and b. Contour plot of the back-flow coefficient in case 1b. Free-stream flow direction: ⇒

The general development of the back-flow coefficient, χ, follows, as could be expected, the average flowfield development. Notice that χ=50% coincides very well with U=0 even away from the plate. Here it is, however, more clear how unstable the separated region is, despite of the trip. The height of the separated region clearly varies a great deal over time. The disturbances in the 715-735 mm range are due to smoke fluid stuck on the plate surface, which has resulted in an uneven light sheet and imprecise measurements in that region.

3.2. Separation bubble

When a separation trip in the form of an aluminium strip that was taped to the plate along its front edge and rested on a thick layer of tape so that its rear edge was about 8 mm above the plate, was introduced at x=0.67 m in case 3, a limited separated region following the trip was established. In this case, referred to as case 2, there was significant back-flow, so hot-wire measurements could not be undertaken. Therefore, the following data were obtained exclusively with PIV.

velocity field, 1 mm=5 m/s, n=170

velocity field, 1 mm=5 m/s, n=223

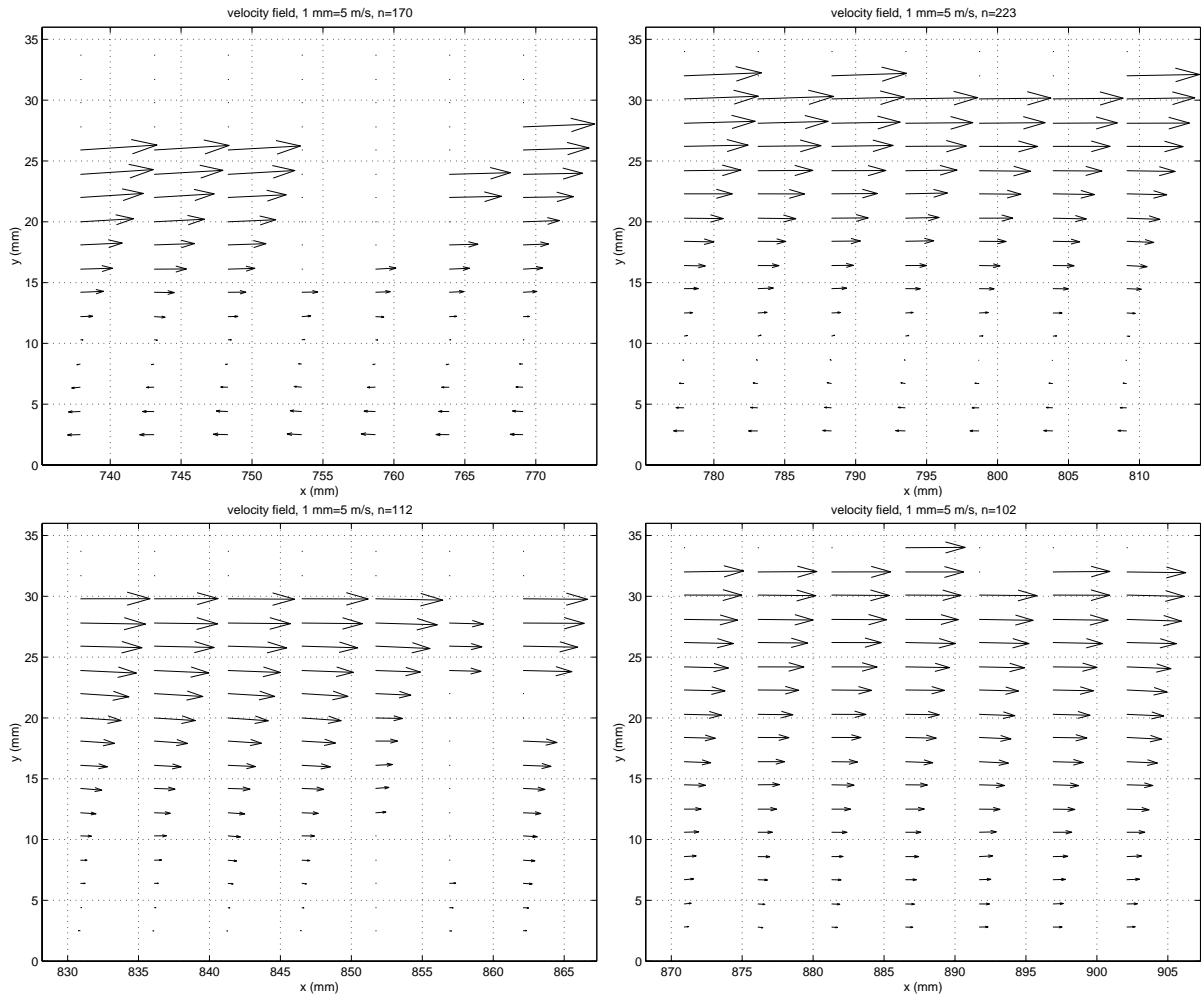velocity field, 1 mm=5 m/s, n=112

velocity field, 1 mm=5 m/s, n=102

Figure 13a, b, c and d. The four figures above show the average flow field in and above the rear part of the separation bubble. Free-stream flow direction: ⇒

In figure 13, the number of displayed velocity vectors have been reduced through averaging over areas covering three interrogation areas in the vertical direction and eight in the horizontal direction. The shadow of a thread below the plate made valid measurements around x=855 mm impossible. Figure 13 clearly shows a region of back-flow about 10 mm thick following the separation trip. The n number given above each of the vector plots in figure 13 is the number of frame pairs that were taken in each area. In this case, the number of pictures taken was sufficient to give an accurate average velocity field.
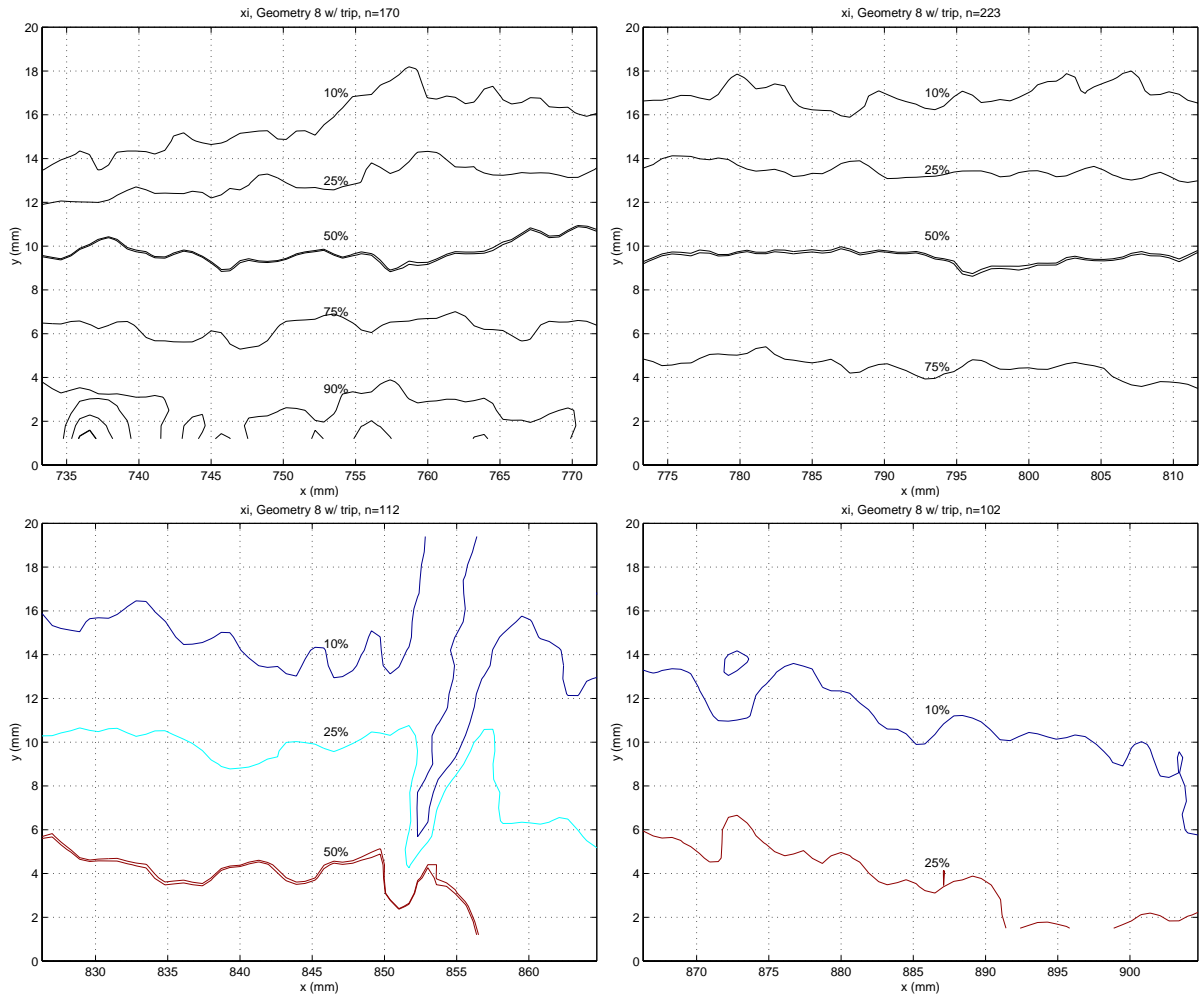
- 20 -

Figure 14a, b, c and d. The four above figures show the back-flow coefficient in four consecutive PIV areas. The lines correspond to 10, 25, 50 (double), 75 and 90% back-flow. Free-stream flow direction: ⇒
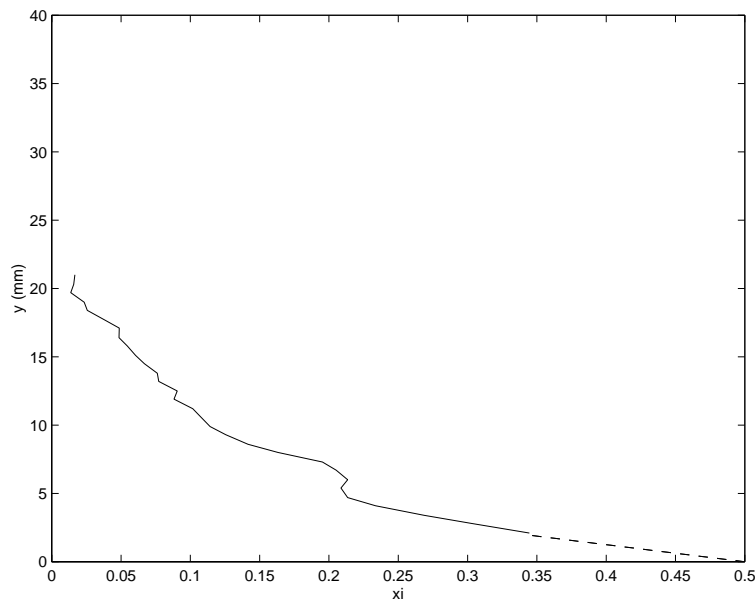

Figure 15. The back-flow coefficient χ(y) at x=0.882 m, the approximate position of mean reattachment.

The back-flow contours given in figure 14 above are based on velocity data which have been validated, averaged and then smoothed in space to give a clearer picture. The contours give an indication of the size and shape of the separated region. The region with >50% back-flow

seems to be about 10 mm high and have a tapered rear end. The position of reattachment fluctuates a great deal along the plate, but the position of mean reattachment seems to be close to x=0.88 m. Figure 15 shows the χ profile at this x-position. When the flow reattaches to the plate, the wall shear stress is zero and the back-flow, according to Dengel and Fernholz [9], is 50%. According to their study, this point coincides with the point where the shape factor H is 2.85. As is shown in figure 16, the present study gives a somewhat higher value of H at reattachment – 3.1<H<3.4 in the 0.877<x<0.887 range. This discrepancy might be due to the PIV measurements being obtained some distance away from the wall. The closest point to the surface in the studied configuration is at y=1.2 mm, where the velocity value is really an average of the flow velocities in the y=-0.1 - 2.5 mm range. As Dengel and Fernholz showed, the back-flow coefficient may vary dramatically close to the wall. This is also demonstrated in figure 15.
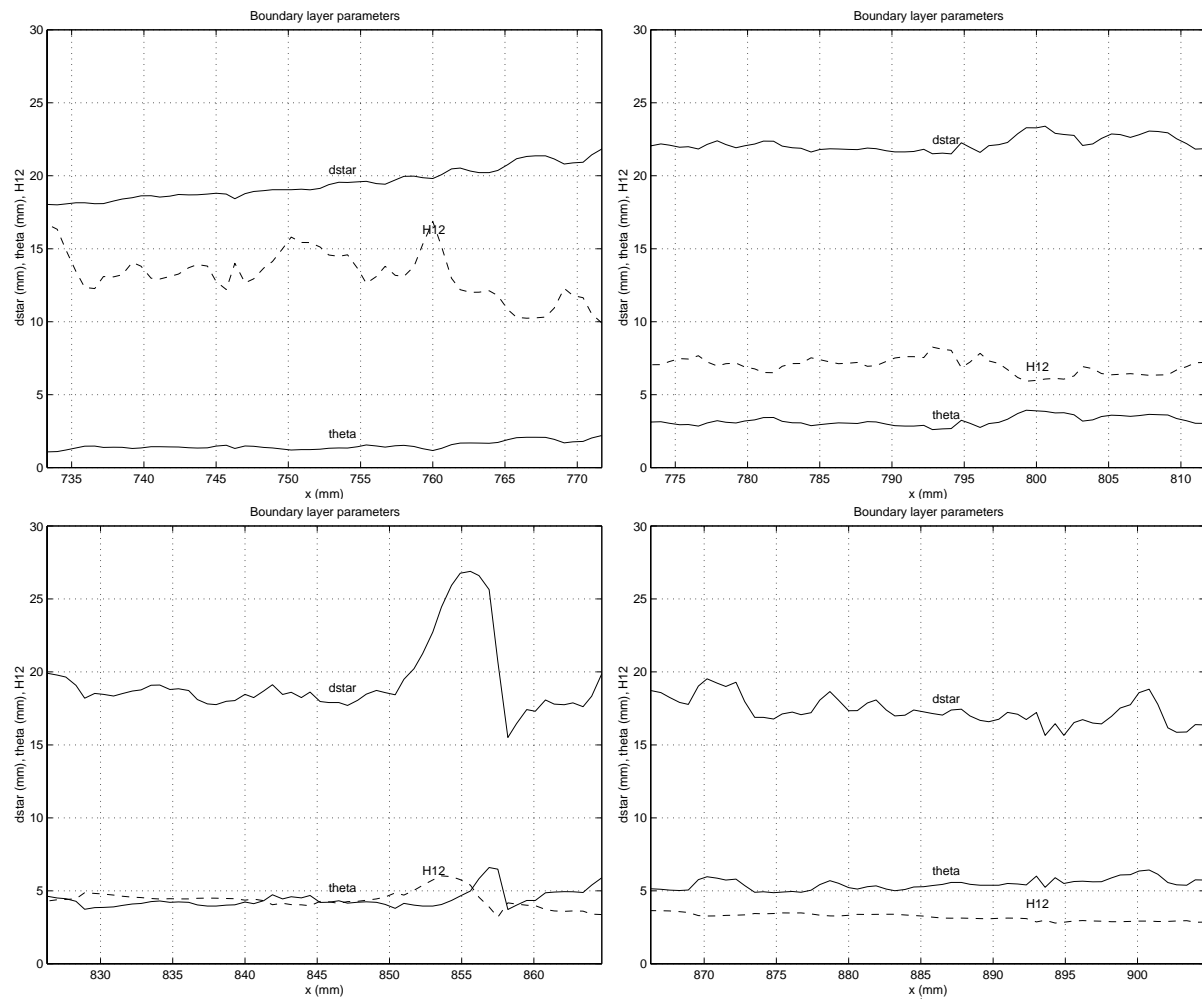

Figure 16a, b, c and d. The four figures found above show how the boundary layer parameters, δ^*, θ and H, vary in and after the separation bubble. Free-stream flow direction: ⇒

As can be seen in figure 16, the shape factor H reaches a very high value in the separated region. This is due to the fact that the reversed flow region close to the plate gives high values for $(1-U/U_\infty)$ and negative values for $U/U_\infty(1-U/U_\infty)$, which results in a high δ^* and a low θ. While θ increases slowly throughout the studied region, δ^* decreases towards the rear of the bubble and during the reattachment.

Figure 17 shows what the velocity profiles U(y) look like in the in the separated region and following reattachment.
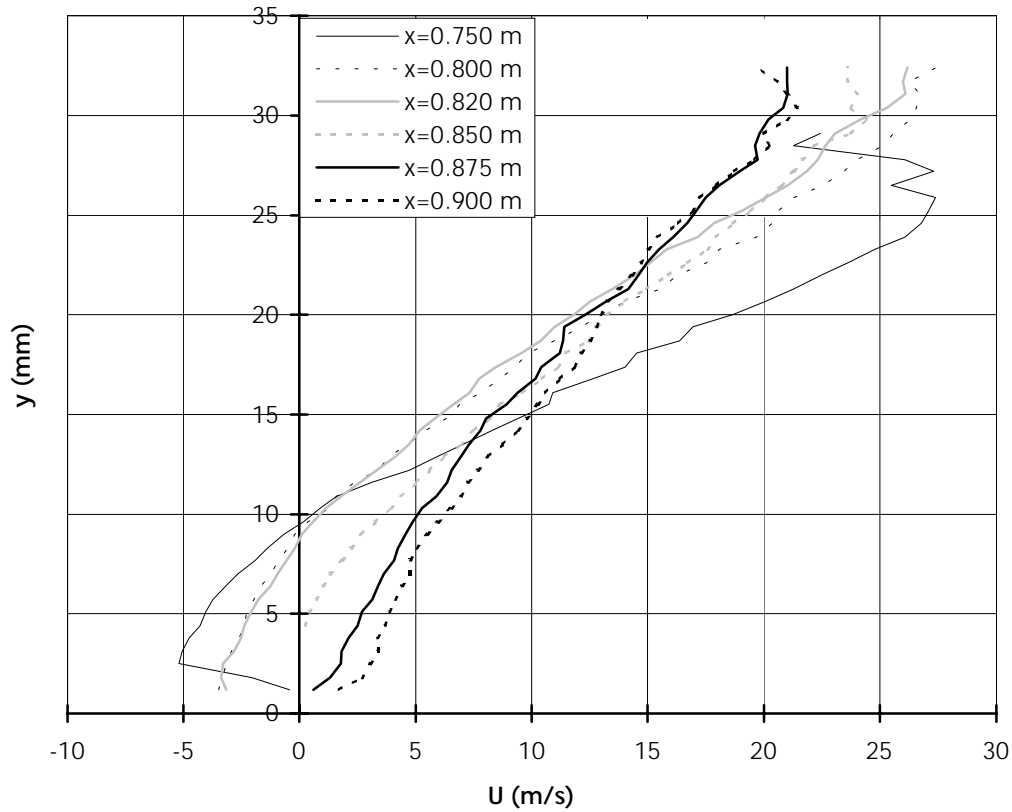
Figure 17. The above figure show velocity profiles in the boundary layer at 7 different x-positions that have been acquired through use of PIV in case 2.

3.3. Attached boundary layer

In case 3, the boundary layer remained attached to the plate everywhere, despite the imposed adverse pressure gradient. In this case, the absence of back-flow meant that a conventional hot-wire probe could be used to acquire velocity profiles and plots of the perturbation velocity moments. Velocity profiles were taken at 5 different x-positions, x=0.577, 0.645, 0.700, 0.775 and 0.850 m. In addition, PIV measurements were made in the 0.745<x<0.790 m region. These will be discussed in section 4.2.

<u>Mean-velocity profiles and boundary layer development</u>

The applied adverse pressure gradient leads to the expected deceleration of the flow in the boundary layer. This is shown in figure 18.
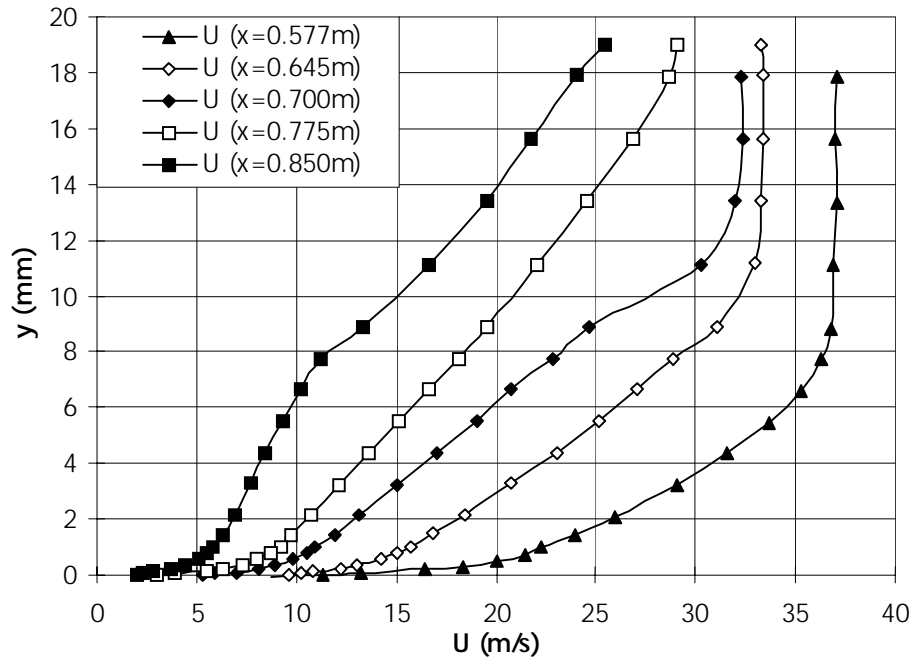
Figure 18. Mean velocity profiles for case 3.

The deceleration is most evident in the near-wall region and it makes the profiles lose fullness and gives them an increasing shape factor H. The increase in the total boundary layer thickness is so large that the hot-wire mount used in this experiment could not be traversed far enough away from the plate at the two most down-stream positions to reach the free-stream. Therefore, PIV measurements were used to acquire the free-stream velocity and approximate velocity profiles. From these corrected velocity profiles, parameters like δ^*, θ and H were computed along with the flux per unit width of the wind tunnel as $U_\infty(h-\delta^*)$ and the results are presented in the table in table 1. The fact that the flux does not seem to decrease in the down-stream direction, as would be expected when the removal of flow through the ceiling is taken into account, indicates that the suction is insufficient to remove all of the ceiling boundary layer or that the expansion or the suction is so strong that there is not enough time for an even velocity profile in the y-direction to develop. At the two most downstream positions, the free-stream velocity could not be measured with the hot-wire mount used, so these velocities were extracted assuming constant flux throughout this region. PIV measurements near the outer edge of the boundary layer indicates this approach to be successful, even though the second suction box does not end until somewhere around x=0.75 m. Apparently, the amount of air removed after x=0.70 m is negligible.

x (m)	0.577	0.645	0.700	0.775	0.850
Uo (m/s)	37.1	33.4	32.4	29.4	28.1
δ^* (mm)	1.637	2.963	4.663	6.325	9.300
θ (mm)	1.009	1.728	2.284	3.166	3.776
H	1.541	1.675	1.990	1.963	2.421
flow (m²/s)	4.46	4.40	4.77	4.77	4.77

Table 1. This table shows the variation of different parameters along the plate in case 3.

As table 1 shows, both the displacement and the momentum thickness grow almost linearly with x in this case. The shape factor rises in the down-stream direction, but not high enough to suggest mean flow separation.

Wall shear stress measurements

The pressures measured by the Preston tube were compared with the static pressures at a number of different positions. According to Bertlerud, the calibration formula (1) should be more accurate than Preston's original calibration curve for Preston tubes within the logarithmic region of the boundary layer as long as $2.5 \cdot 10^3 < \Delta p D^2/(\rho v^2) < 2.1 \cdot 10^8$. For the present conditions, this means that the measured pressure differences must be in the $1 < \Delta p < 86000$ Pa range. Another condition that has to be fulfilled controls the non-dimensional pressure gradient p^+:

$$p^+ = \frac{v}{\rho u_\tau^3} \frac{dp}{dx}$$

According to the survey of earlier studies by AF [1], there should be a logarithmic layer in the boundary layer as long as p^+ is smaller than approximately 0.03. According to figure 19, using Preston tubes and static pressure taps, this critical value of p^+ is reached somewhere around x=0.7 m in case 3. AF noted that using the zero pressure gradient scaling of boundary layers to calculate the friction velocity gave wall shear stress results that differed significantly from wall shear stress obtained from pulsed-wire velocity measurements close to the wall.
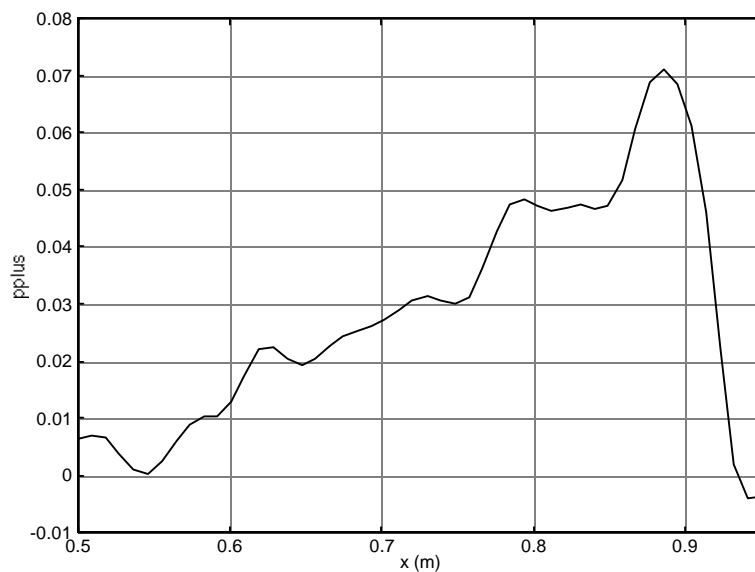

Figure 19. Variation of the non-dimensionalised pressure p^+ along the plate in case 3.

However, if a similarity exist for the velocity profiles near separation one may hope to find a calibration curve that links Preston tube dynamic pressures with wall shear stresses even in the absence of a logarithmic wall region. The measured zero difference pressure should anyway indicate zero average velocity, i e the separation point. In the back-flow region, Preston tube measurements are meaningless, and will be wrong as soon as there is intermittent separation.

Figure 20 shows hot-wire velocities plotted in wall co-ordinates, where the friction velocity u_τ is chosen so that a maximum fit is established with the empirical log law $u^+=5.6 \log_{10} y^+ + 4.9$. As is clearly seen in figure 20, there is a distinct logarithmic layer at all x-positions. However, it seems like the logarithmic layer moves inward for high shape factors, but even at

- 25 -

x=0.85 m, where $p^+=0.05$, the logarithmic layer apparently stretches out to at least $y^+=40$, which corresponds to y=1.2 mm.
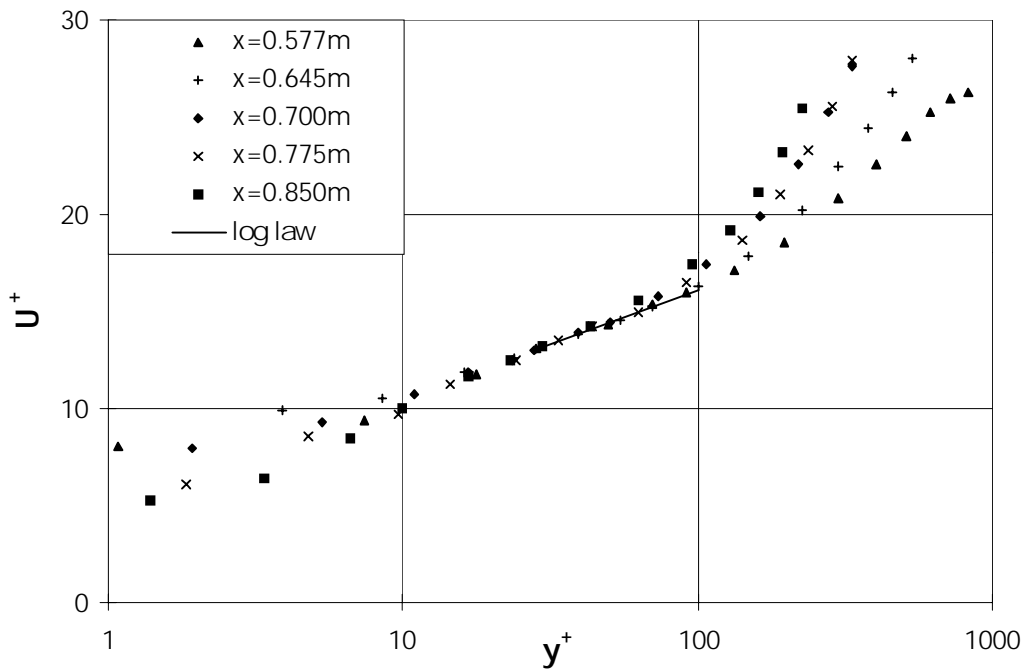

Figure 20. Mean velocity profiles for case 3 plotted in wall co-ordinates.
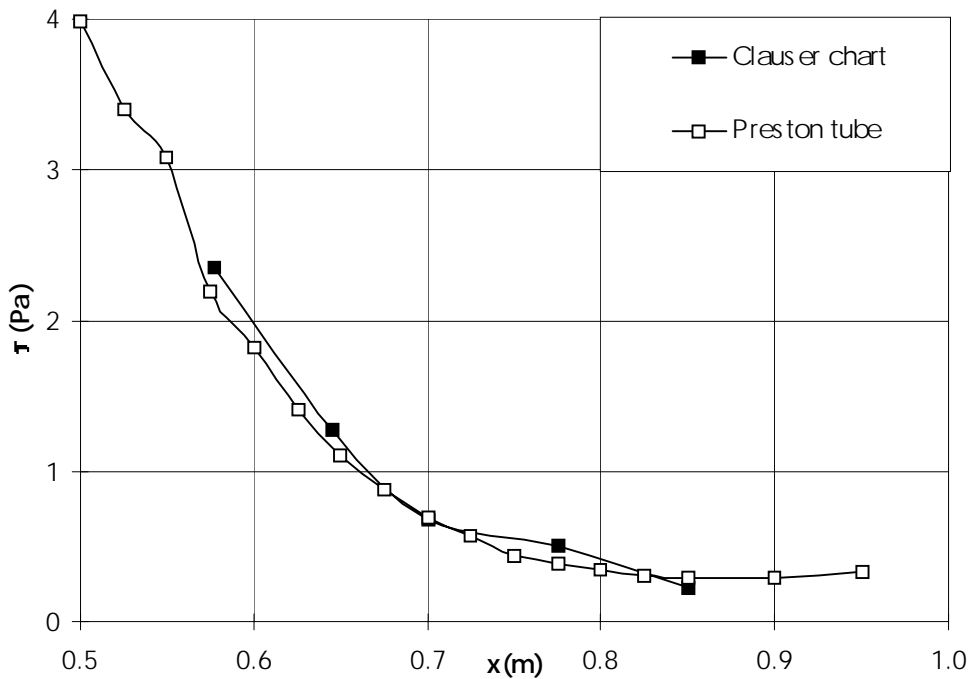

Figure 21. Wall shear stress in case 3.

The wall shear stresses as measured by two different methods, the Preston tubes and the Clauser plot in figure 20, are shown in figure 21 to be similar.

Skåre and Krogstad [27] found a general tendency of the Clauser plots giving lower values of the skin friction than Preston tubes. This was not confirmed in this investigation. This may be a result of Skåre and Krogstad using the Patel calibration curve for the Preston tube measurements instead of the Bertlerud calibration curve that was used in this examination. In the range of wall shear stresses encountered in SK's experiment when H=2.0, Patel's curve tends to give values of the wall shear stress 0-10% above those given by Bertelrud's formula. Since the deviation from the Clauser plot wall shear stresses in SK's experiment is in this order, this suggests that Bertelrud's formula works better than Patel's in that case.

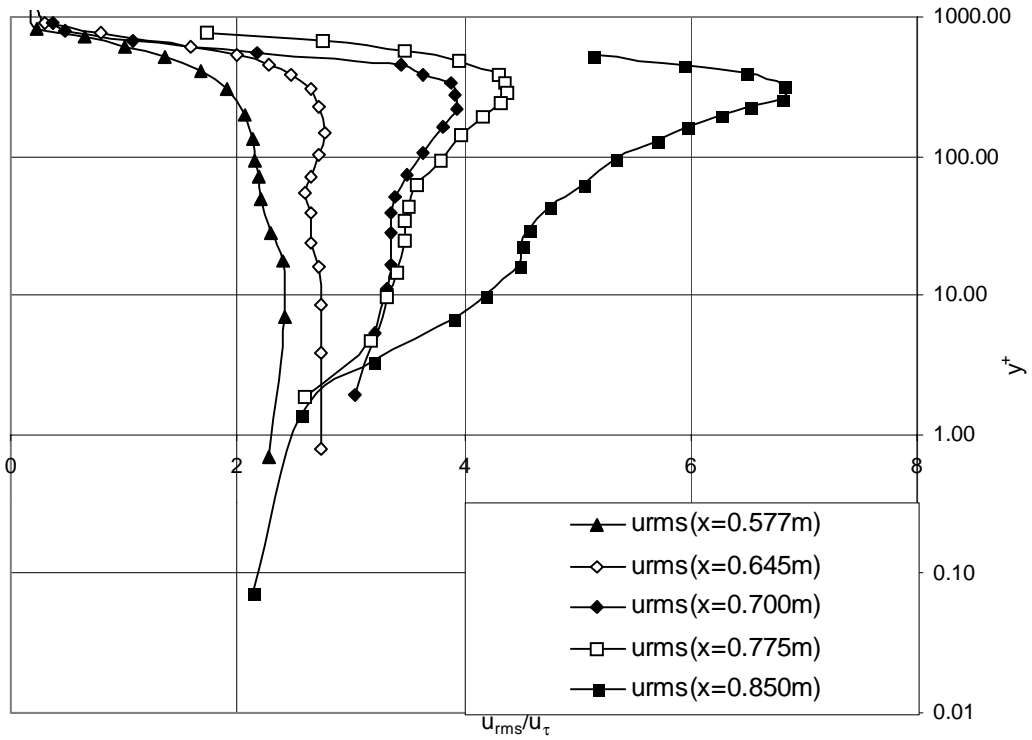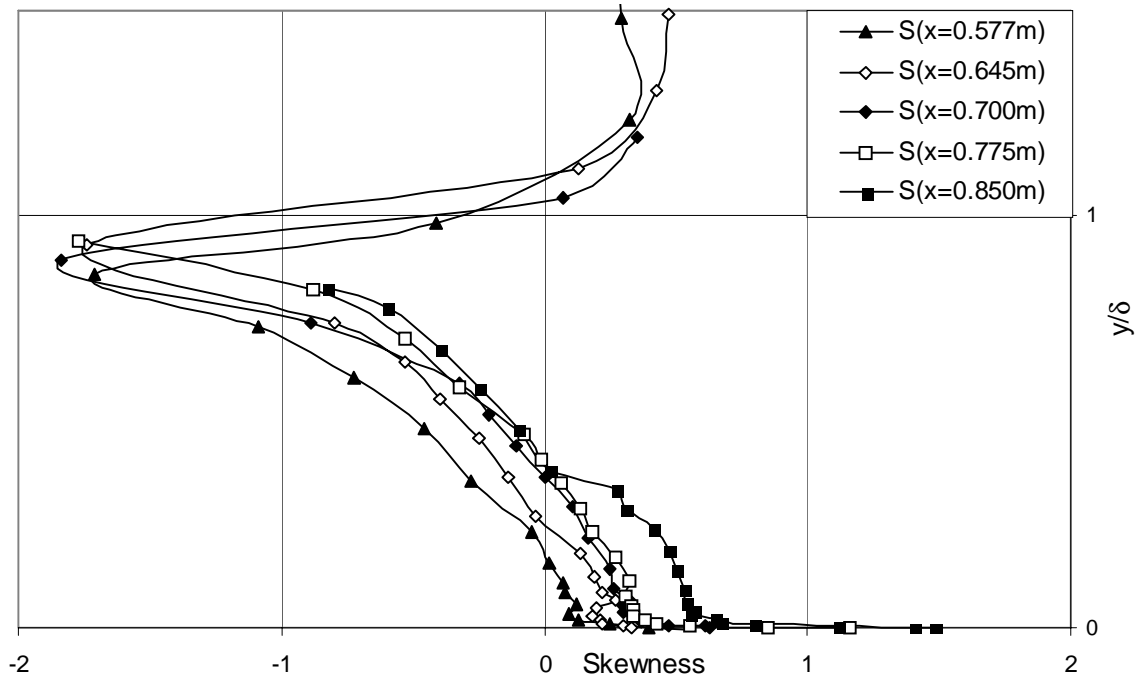### 3.4 Turbulence statistics in the attached boundary layer
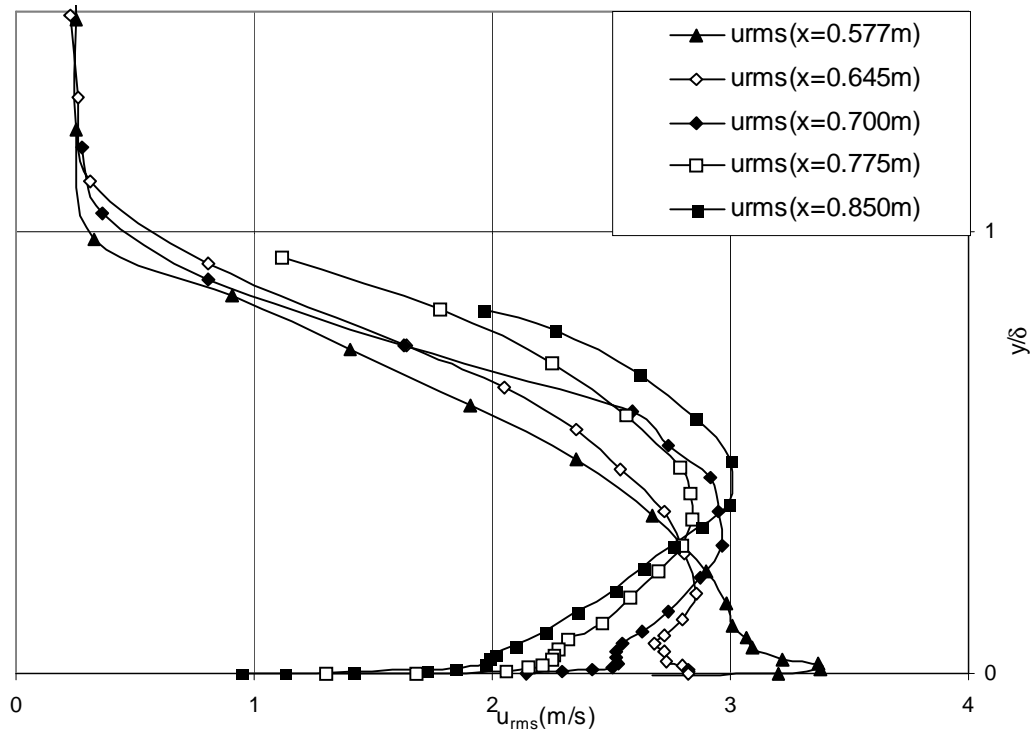
Figure 22a and b. Velocity variation, u_{rms}, profiles for case 3 in outer and inner scales, respectively.
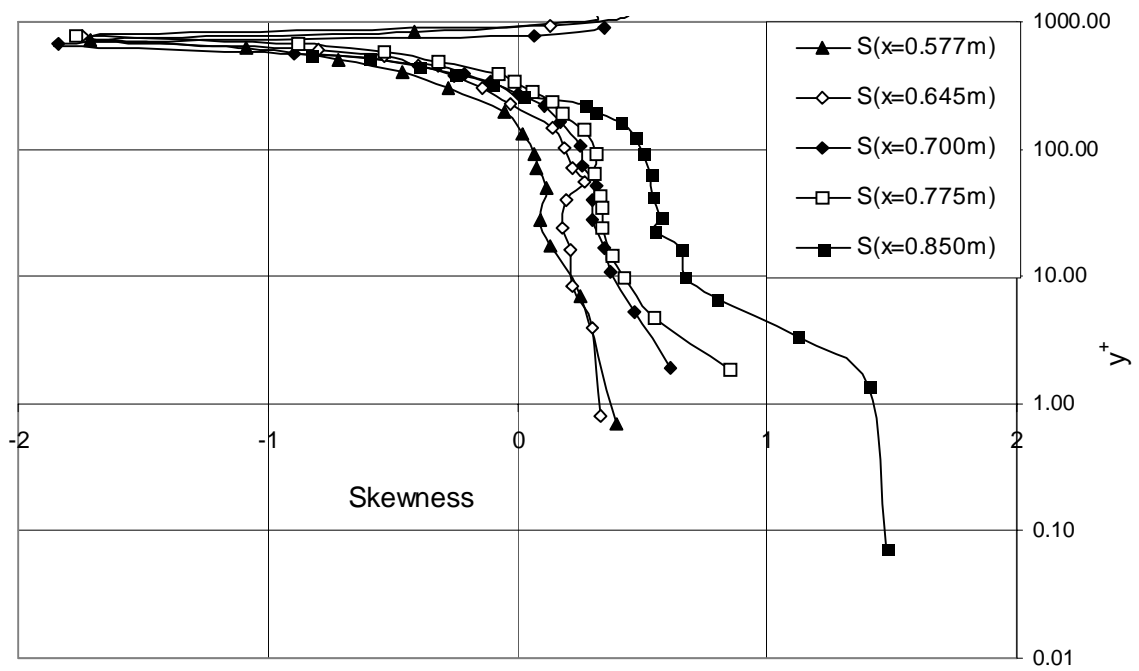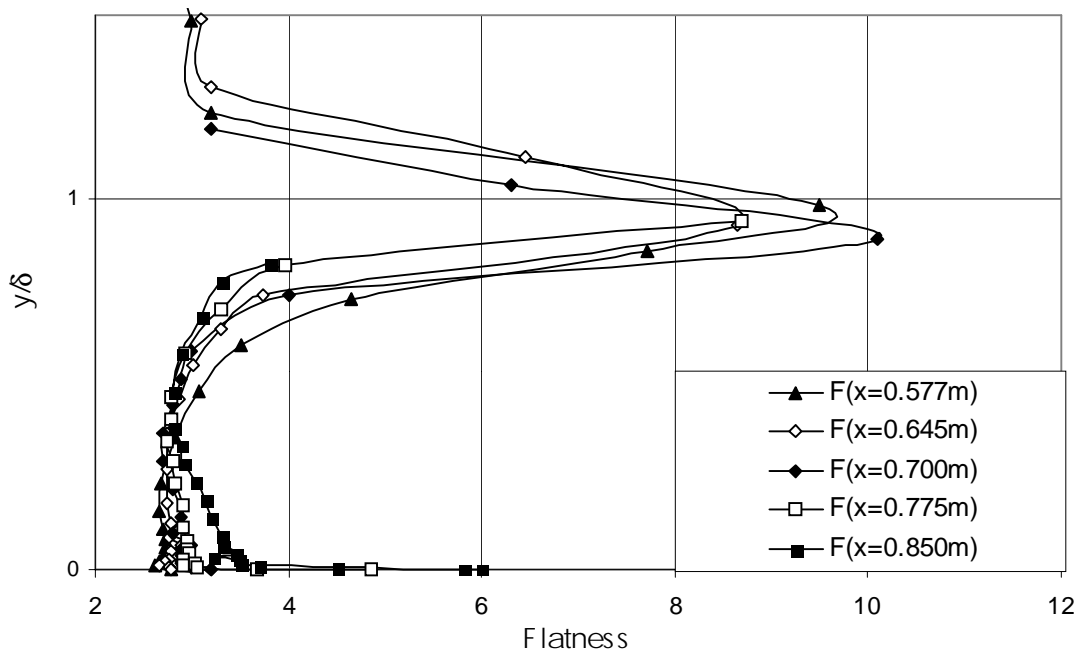
Figure 23a and b. The skewness of the streamwise velocity in case 3 in outer and inner scaling.
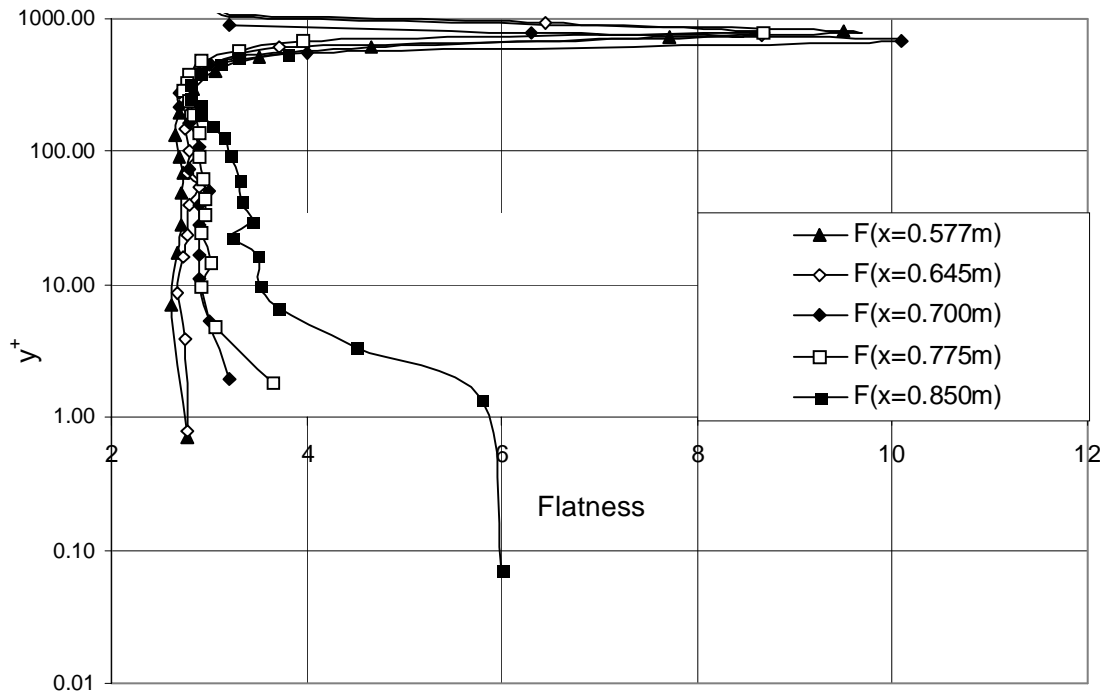
Figure 24a and b. The flatness of the streamwise velocity in case 3 in outer and inner scaling.

The measurements of u_{rms}, skewness (S) and flatness (F) of the stream-wise velocity component in the present investigation have been compared with the results of some earlier experiments. To facilitate the comparison between the different investigations, the ranges of a couple of dimensionless boundary layer parameters are given in table 2.

	Re_θ(min)	Re_θ(max)	$\theta dCp/dx$(min)	$\theta dCp/dx$(max)
G	2867	7227	13	40
AF	2849	7524	0	6
DF	1468	10800	3	47
SK	1351	80600	0.87	3.6

Table 2. Different parameter ranges in the present experiment (G) and in those by Dengel and Fernholz (DF)[9], Alving and Fernholz (AF)[2] and Skåre and Krogstad (SK)[27].

Outer region

As figures 22-24 indicates, the outer region of the boundary layer, $y/\delta \approx 1.0$, is characterised by sharp peaks in both S and F, while u_{rms} smoothly approaches its free-stream value. One may note that from the few free-stream measurements available, it seems like u_{rms} in the free-stream remains constant despite a decreasing mean velocity, giving an increase in the turbulence intensity, $Tu \equiv u_{rms}/U_\infty$, of the free-stream in the downstream direction. The peaks in S and F seem to be located near $y/\delta=0.9$ and the peak values reached, $S \approx -1.8$ and $F \approx 10$, seem to be constant in the down-stream direction.

The existence of an outer peak in S and F is confirmed by Alving and Fernholz (AF) [2], who at H=2.39 found a peak S of –2.3 at $y=\delta$ and F>8 for $y/\delta>0.8$ (the actual peak value is not evident in their plot).

Dengel and Fernholz (DF) [9] also found a peak in S close to $y/\delta=0.9$ and in F in the region $0.9<y/\delta<1.0$, but unlike the present investigation, DF found the peaks to grow with increasing shape factors. At H=2.4 the peak values were S=-1.7 and F>8.

In Skåre and Krogstad (SK) [27], an equilibrium boundary layer with H=2.0 was examined. They found a skewness peak near $y/\delta=0.9$, where S reached values of the –2.0 to –2.5. The flatness peak was located close to $y/\delta=0.85$ and attained values around F≈9.

In summary, one can conclude that the present study is in general agreement with earlier examinations in this area. While all studies have found peaks in S and F around $y/\delta=0.9$, the peak values attained show much greater variation and clearly do not depend solely on the shape factor.

Centre region

Figures 22-24 show that the centre portion of the boundary layer is characterised by a smooth maximum in u_{rms} as well as a shift from negative to positive skewness as one moves inward. The flatness in this area reaches a minimum close to the gaussian value of F=3 as one moves inward from the outer peak. As one moves in the downstream direction of the boundary layer, the position of the u_{rms} peak moves away from the wall as the shape factor H increases. At H=1.68 it is located at $y/\delta=0.18$, while it has reached $y/\delta=0.44$ at H=2.42. At low values of H, it merges with the inner peak, which will be discussed in the next section. The value of u_{rms} at the peak increases from 8.5% of U_∞ at H=1.68 to 10.7% at H=2.42. The position of zero skewness moves outward in a similar manner, from $y/\delta=0.18$ at H=1.54 to $y/\delta=0.35$ at H=2.0, but unlike the u_{rms} peak, it remains at an almost constant y/δ position as H increases above 2.

AF [2] found a similar trend in the u_{rms} position – it moved from $y/\delta=0.36$ at H=1.9 to $y/\delta=0.61$ after separation where H=3.2. Upstream of separation at H=2.39, the u_{rms} peak was found at $y/\delta=0.47$ where S=0 was also found. They also examined how S varied after reattachment, and found the S=0 y/δ-position to move closer to the plate as H decreased. u_{rms}/U_∞ rose slowly with increasing shape factors, but remained about 20%.

For strongly decelerated, but attached flows with H=2.5-2.8, DF [9] found u_{rms} to peak near $y/\delta=0.6$, where S also became zero and F reached a minimum. The quota u_{rms}/U_∞ was about 20% at the peak, increasing slightly with growing H, in agreement with AF's observations.

In SK's [14] examination, where H=2.0 throughout, the maximum u_{rms} was found at $0.35<y/\delta<0.45$. At this peak, $u_{rms}\approx0.12U_\infty$. In the numerical investigation of Henkes, Skote and Henningson (HSH) [12], the peak u_{rms} was found at $y/\delta=0.48$ for a boundary layer similar to that of SK's experiment, H=2.0. Due to the low Re_θ accessible to the DNS, the peak is smoother than that found in SK's experiment.

The positions of the u_{rms} peak and S=0 seem to be located somewhat closer to the plate in the present investigation than in the earlier investigations, even though the trend that the positions move towards the outer boundary layer as H increases is clear. Another difference between the present investigation and earlier experiments is the much lower value of u_{rms}/U_∞ attained at the peak in the present experiment, especially when comparing with the experiments by AF and DF. The position of the outer u_{rms} peak seems to, at least approximately, coincide with S=0 and the minimum of F, just like in ZPG boundary layers.

<u>Near-wall region</u>

In the region close to the plate, the flow changes radically as the wall shear stress is reduced. Figures 22-24 show that while the sharp peak in u_{rms} that is also found in ZPG flows disappears as H increases, sharp peaks in skewness and flatness develop in the $y^+<10$ region. Below $y^+=1$, S=1.5 and F=6 at the most downstream position, where H=2.4. At the most upstream x-position, where H=1.54, the u_{rms} peak value is $2.5u_\tau$. The near-wall ($y^+<2$) u_{rms} remains in the $2-3u_\tau$ region even at higher H, where the peak disappears.

While the resolution of the measurements by AF [2] was too low for the entire S and F peaks to be captured, their investigations indicates that there is a region with high flatness close to the wall – F>4 for $y/\delta=0.03$.

DF's [9] investigation was similar to that of AF in that there were no measurements close enough to the plate to describe the skewness and flatness peaks, but the near-wall measurements still indicated the existence of such peaks.

In the experiments by SK [14], the H-value was too high, H=2.0, for sharp inner peaks to be expected. No u_{rms} peak was found in the area $y^+>20$ accessible. S and F was measured as close as $y^+=7$ to the plate, and in these variables, rising values were found as the plate was approached, starting at around $y^+=20$, even though no peak was found. The numerical simulation by HSH [12] disagrees in this region with the SK experiment, which it is supposed to simulate. No near-wall peak at all is found – instead, u_{rms} smoothly approaches zero as the wall is approached, while $u_{rms}=5u_\tau$ in SK's investigation.

In summary, this inner peaks have been much better captured in this investigation than in earlier experiments due to the use of a conventional hot-wire, which makes the near-wall region accessible. Since the highest u_{rms}/U quota was about 0.5, it was concluded that a conventional hot-wire could be used, because back-flow should not occur very frequently under those conditions. This is also indicated by the empirical formula found by Dengel and Fernholz (DF) [9]: H=2.2 + 1.4 χ_w, according to which H=2.2 would be the limit for intermittent separation. The existence of sharp near-wall skewness and flatness peaks in APG flow has later been confirmed through LDV measurements [3] in the same setup (case 3). Compared to SK's investigation, the S and F peaks in the present investigation seem to start closer to the plate, at $y^+=10$ rather than near $y^+=20$.

One observation that indicates that there is no one-parameter (H) family of curves that describe all mean-velocity profiles is that although the shape factors of the profiles measured at x=0.700 and x=0.775 m are almost the same, the profiles are not very similar. The profiles at x=0.577 and x=0.645 m seem to be just as similar even though the difference in H is much larger between those two profiles.

4. Particle Image Velocimetry (PIV)

Since much of the data presented in this report has been collected using particle image velocimetry (PIV), a presentation of this method and its merits and drawbacks when used in this kind of boundary layer study is given below.

4.1. Requirements and features of PIV

4.1.1. General

PIV is a method where particles that are carried by the flow and illuminated by a laser light sheet are photographed twice within a short period of time. The pictures are divided into the same grid of small so-called interrogation areas. The pairs of interrogation areas depicting the same place in space at different times are compared and from the distance that the particles in them have travelled, an average velocity is obtained for each interrogation area. All these velocities put together give a velocity field describing the flow in the entire picture. The pictures are taken with a double-frame CCD camera, specially designed to capture picture pairs with very short intervals between the pictures. Since an entire sheet of the flow can be analysed at once, this technology provides instant 2D data in contrast to point measurement techniques like laser Doppler velocimetry (LDV) and hot-wire anemometry.

4.1.2. Illumination

The short exposure time needed to give a sharp picture of fast-moving particles, means that the illumination of the particles must be very strong during this period. Compared to LDV, PIV requires much higher light densities, because an entire sheet of the fluid is to be illuminated instead of a single point. Furthermore, the measurements are made using light that has been reflected in a direction perpendicular to the laser beam and the reflection in that direction is often much weaker than the back-scattered light that LDV uses. To produce this high-intensity light, a pulsed laser with two cavities, one for each exposure in a pair, has been used in this investigation. In order to obtain data of good quality, it is important that the laser sheets produced by the two cavities are well aligned.

A common problem is that light reflections from solid objects in the flow field, like the plate surface in this case, introduce noise that lower the quality of the data obtained close to the solid objects.

4.1.3. Particles

If good measurement quality is to be attained, there has to be a high particle density throughout the studied region. In the present investigation, the particles to a large extent remained within the boundary layer into which they were released through a slit in the plate. This made the accurate measurement of the free-stream velocity impossible due to the lack of particles there. When there was separation, the smoke tended to break away from the plate, so that the particle density in the back-flow region was much lower than in the area outside of it, even though this seems to be a smaller problem in turbulent separation than in the laminar case, especially for separation bubbles.

In order to obtain good results, it is important to have small particles that follow the airflow closely. But to make the so-called sub-pixel interpolation work well, it is desirable that the particles appear several pixels wide in the digital frames. The purpose of sub-pixel interpolation, which uses the variation of the light intensity over the pixels that are occupied

by a single particle to calculate its centre position, is to increase the velocity resolution beyond that imposed by the pixel size of the frames. According to Dantec's PIV User's manual [11] this should lead to a tenfold increase of the resolution, provided that the seeding is sufficient and the camera setting is such that the particles appear to have the 3-6 pixels diameter recommended. This can, if the particles are too small, be accomplished through defocusing the camera, so that the particles appear slightly blurred. Figure 25 shows an example that clearly demonstrates the discretisation of velocities that PIV may result in when this condition is not met, so that the particles regularly appear just one pixel wide. The flow in the studied area is on the border of mean separation, i e U≈0 m/s, in the middle of the separation bubble in case 2 as figure 2b illustrates. The peaks, which are separated by 2 m/s, correspond to different discrete movements of particles between the two frames. The scale factor, i e the number of pixels per mm in the picture, is 25 and the time between the two frames of a picture pair is 20 μs, which means at that 2 m/s flow velocity the particles move $20 \cdot 10^{-6} \times 2 \times 25000 = 1$ pixel between exposures.
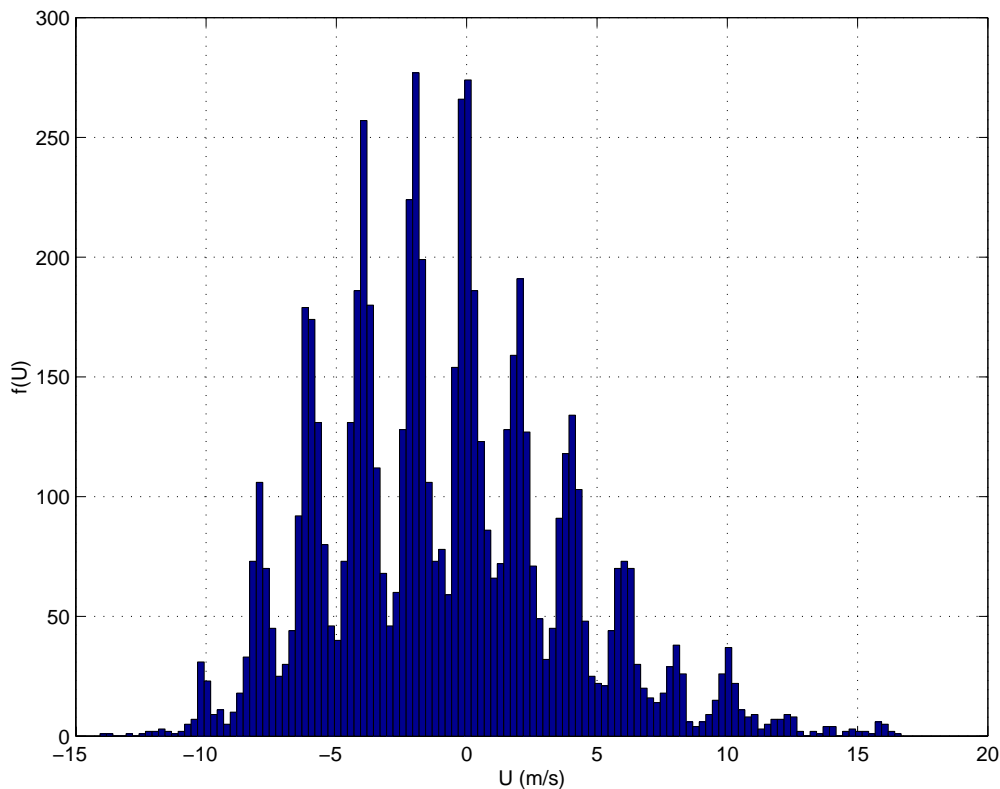

Figure 25. Probability density function – average velocity at y=9.3 mm, x= 774-814 mm in case 2 – demonstrating the PIV discretisation of velocities.

It can also be seen in figure 25 that the velocity is not completely discretised - there are actually a small number of occurrences where velocities between the peaks are found. These probably correspond to particles appearing wider than one pixel for which the sub-pixel interpolation works and gives a continuous distribution of velocities.

When an average of a large number of instantaneous vector fields is calculated, the mean velocity will probably be calculated correctly, but according to simulations, u_{rms} will appear larger and F smaller than they actually are due to the discretisation. A simulation was made, where random numbers having a distribution similar to the distribution in figure 25, except that it was lacking the discretisation. Then U, u_{rms}, S and F were calculated using this distribution before and after a 2 m/s discretisation was introduced. It was found that the

errors produced were small – the discretisation left U virtually unchanged, while u$_{rms}$ became about 2% larger and S about 2% smaller, and F was reduced by about 0.5%. These deviations can be expected to be larger when the standard deviation of the distribution is small compared to the discretisation. Other studies made using PIV at the department indicate that this discretisation, even though less pronounced, may actually cause problems even when the images used are defocused so that the particles appear sufficiently large for the sub-pixel interpolation to work. The reason for this is not known.

A closer look on the velocity distribution than in figure 25 reveals that there is another velocity discretisation as well. This discretisation, which is 1/16 m/s in the examined case, seems to be caused by some truncation of binary decimals when the velocities are calculated or stored. In this case it is not as severe a problem as the much coarser discretisation caused by the failure of the sub-pixel interpolation.

4.1.4. Resolution

The resolution of PIV in the current investigation is limited by the fact that there must be a number of particles, typically 5, must be present in each interrogation area if reliable measurements are to be attained [14]. In the current investigation, the interrogation areas over which an average velocity is computed, had to be 64x64 pixels large, in order to regularly contain that many particles. Because of these relatively large interrogation areas – at x=0.7 m in case 3 they have a side length of 0.5 δ^* – the strong velocity gradients of a boundary layer in the sheet cannot be captured accurately.

4.1.5. Time

The movement of the particles can only be tracked as long as they remain within the same interrogation area during both exposures. It is recommended [11] that particles should not traverse more than one fourth of the side length of the interrogation areas between exposures to keep the number of particles that leave the interrogation area down. At low seeding densities, even shorter time between exposures or larger interrogation areas should be used to keep the errors that are introduced when particles leave their interrogation area to an acceptable level. Hence the time between the two frames must be very short, some microseconds in the present case. The higher the flow velocity and the smaller the interrogation areas, the shorter time is required between the two frames. In areas with velocity gradients, as the boundary layers studied here, the time interval must be chosen so that enough particles in the relatively high-speed free-stream remain within their interrogation areas. This means that particles in the inner region of the boundary layer, where the velocity is much smaller, move just a very short distance between the frames. Since the discretisation provided by the camera frame pixels, even with sub-pixel interpolation working, also discretise the attainable velocity values, and at small flow velocities, this discretisation may be a severe limitation to the accuracy of PIV. This problem could be solved if elongated interrogation areas, which allow a good resolution of the boundary layer in the wall-normal direction while being long enough in the mean-flow direction to allow the rapid particles of the free-stream to stay within the area between exposures. However, as figure 10 shows, the vertical velocity component in instantaneous velocity fields is not necessarily small compared to the horizontal component. Another option would be to take more than two pictures in a series after one another, so that picture pairs with different time differences could be chosen for interrogation areas with high and low flow velocities.

When there is a velocity gradient in the studied region of the flow, a couple of new problems arise, apart from the problem of choosing the right time between the frames that was discussed above. Firstly, since the velocity of the particles in a single interrogation area will vary depending on their position within the area, it will be harder to find the correct average velocity since the velocity peak found during the spatial cross-correlation is less sharp. Secondly, if there are particles travelling with different velocities in an interrogation area, those that have the highest velocity are more likely to leave the area during the time between exposures than slower particles are. This means that the velocity measured will tend to be lower than the actual average velocity within the interrogation area. Measurements by Keane and Adrian [14] indicate that the calculated velocity vector will be correct in 95% of the cases, if the following condition is fulfilled:

$$\frac{\Delta u \Delta t}{Sd} < 0.03,$$

where Δu is the maximum mean deviation from the average velocity in an interrogation area, Δt is the time between exposures, S is the object-to-image scale factor, i e the physical length corresponding to one pixel in the picture, and d is the side length of the interrogation area in pixels.

4.2. Disturbances caused by the hot-wire mount

Since the mount which is used in the hot-wire measurements is not infinitesimally small, it will affect the flow. To estimate the influence of the mount on the flow field, a series of PIV measurements were made for case 3 with and without the hot-wire mount in position. The below picture shows how this study was conducted, but obviously, the sensitive hot-wire could not be in the wind tunnel while the PIV measurements were taken because the smoke particles would damage the wire, so the measurements have been made with a dummy hot-wire mount in place.
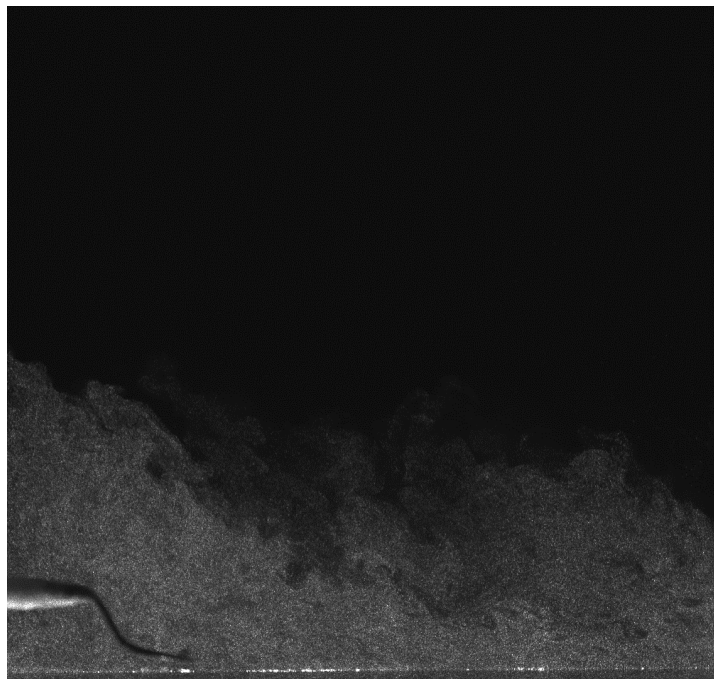

Figure 26. The above picture shows the x=745-785 mm range with the hot-wire clearly visible at the left end of the picture and the surface of the plate at the bottom.
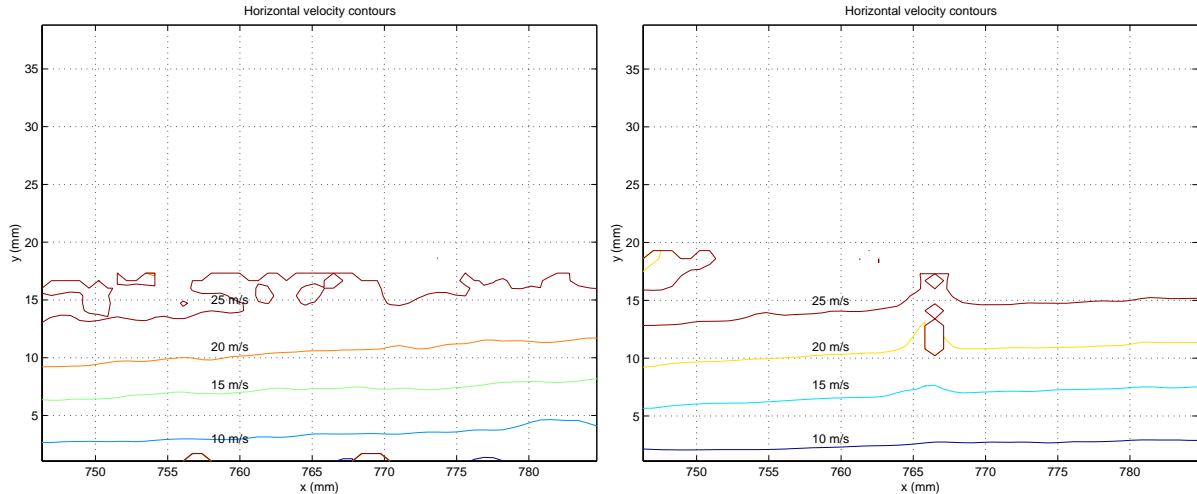
Figure 27a and b. The above two pictures show horizontal velocity contours in the same area with and without a hot-wire mount, respectively.

As can be seen, in figure 27 above, the differences produced when introducing the hot-wire mount are not very large. Most notably is that the near-wall velocities seem to have decreased somewhat thanks to the introduction of the hot-wire mount. No data can be produced for the free-stream because of the lack of particles there and this is also the reason for the jagged 25 m/s-contour. The 106 and 288 picture pairs taken with and without the hot-wire mount, respectively, are insufficient to give smooth and reliable velocities. To achieve a higher data quality, average mean velocity and u_{rms} profiles were calculated using 10 and 20 points in the x-direction around x=0.775 m in the two cases. This corresponds to averages over 6 and 12 mm in the x-direction, which is acceptable in a flow that evolves this slowly in the x-direction.
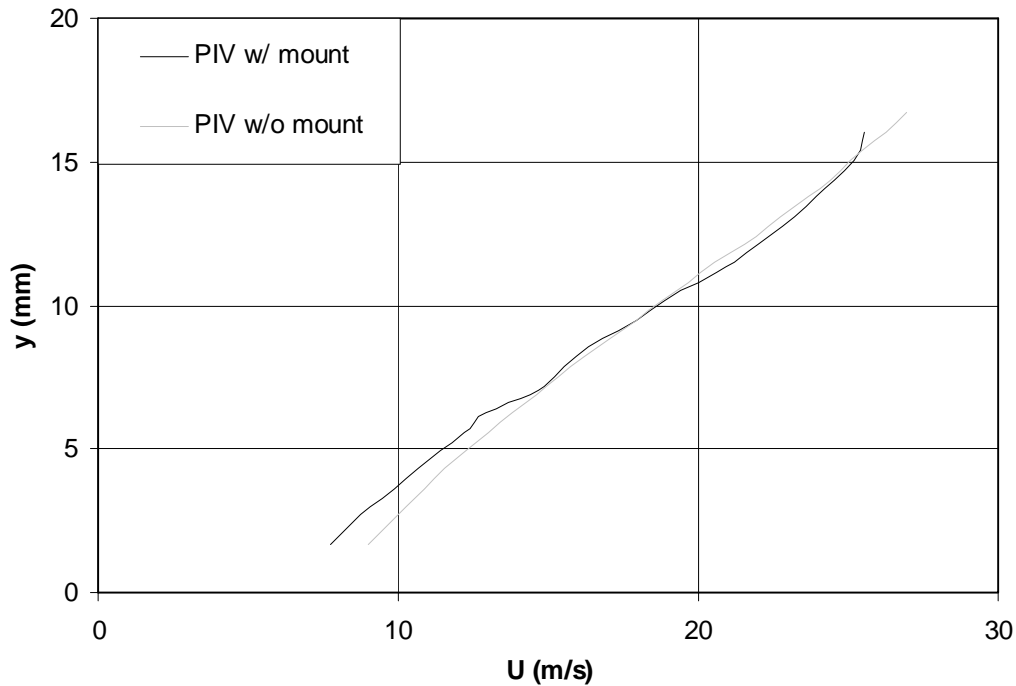

Figure 28. Velocity profiles obtained using PIV at x=0.775 m, with and without the hot-wire mount in position.

According to figure 28, the hot-wire mount retards the flow out to y=7 mm. At y=2 mm, the difference in velocity between measurements with and without the hot-wire mount in position is about 1 m/s and the effect diminishes gradually at higher y-values.
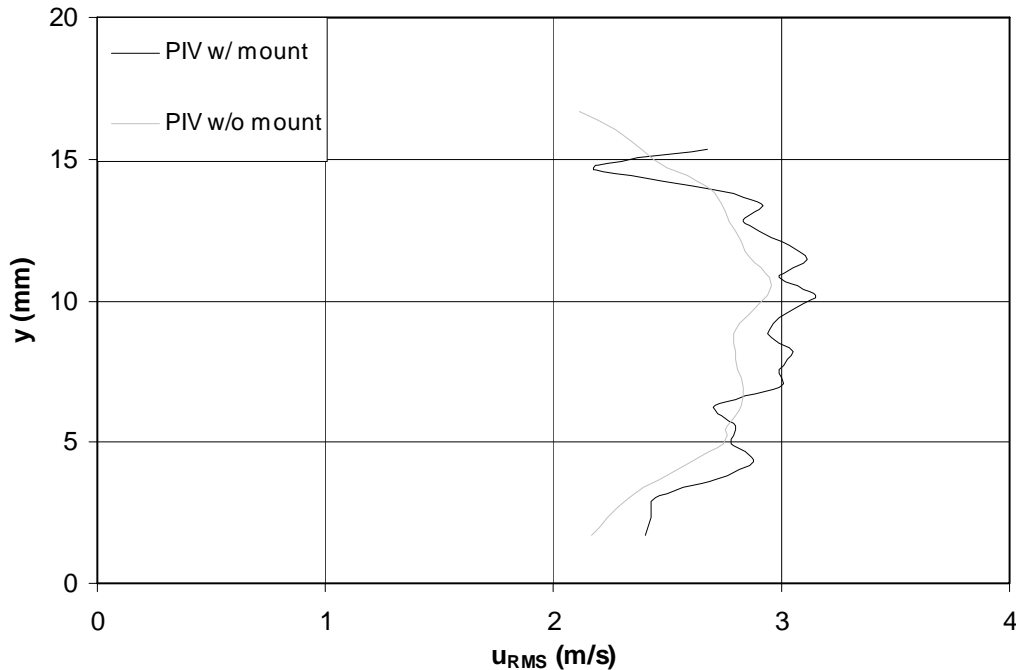

Figure 29. In this figure is shown a comparison of PIV measurements of u_{rms} around x=0.775 m with and without the hot-wire mount in position.

Figure 29 suggests that the introduction of the hot-wire mount produces a small increase in the u_{rms} near the plate. Below y=10 mm, the increase seems to be about 0.2 m/s. The fact that the u_{rms} varies erratically in the y-direction despite the fact that they are averages of measurements at several x-positions discourages from calculating higher order moments using PIV in this case. A far greater number of picture pairs would be needed to get accurate values of skewness and flatness.

Close to the plate, PIV measurements cannot compete with hot-wire data, due to the low resolution. In this case the apparent resolution is 0.65 mm, but each velocity vector given corresponds to an average velocity in a 2.6 x 2.6-mm area. Averaging of velocities over such a large area is also particularly detrimental in regions with strong velocity gradients; where too low values of U and too high values of u_{rms} are to be expected.

5. Scalings

Several different non-dimensional scalings of the mean velocity profiles U(y) have been suggested. The idea behind these scalings is to find a family of curves that describes how the boundary layer develops in an adverse pressure gradient. Then the parameters that describe these families are used to find general relations that predict the wall shear stress and separation position of boundary layers developing under different conditions.

5.1 Clauser scaling

One scaling that was suggested by Clauser in 1954 [7] deals with so-called equilibrium boundary layers. The velocity profiles U(y) for these layers fall on top of oneanother for all x-positions when they are scaled according to:

$$\frac{U - U_\infty}{u_\tau} = f(\frac{y}{\delta})$$

Only a specific family of pressure distributions leads to equilibrium profiles. Unlike the laminar case, where H remains constant for equilibrium profiles (the so-called Falkner-Skan profiles), H varies slightly with Re_x for self-similar turbulent boundary layers. According to Clauser, the equilibrium turbulent boundary layer that gives minimum wall shear stress without separation occurring results when the free-stream velocity varies according to $U_\infty \propto x^{-0.29}$.

As is shown in figure 30, the pressure distribution that was used in case 3 gave non-similar velocity profiles.
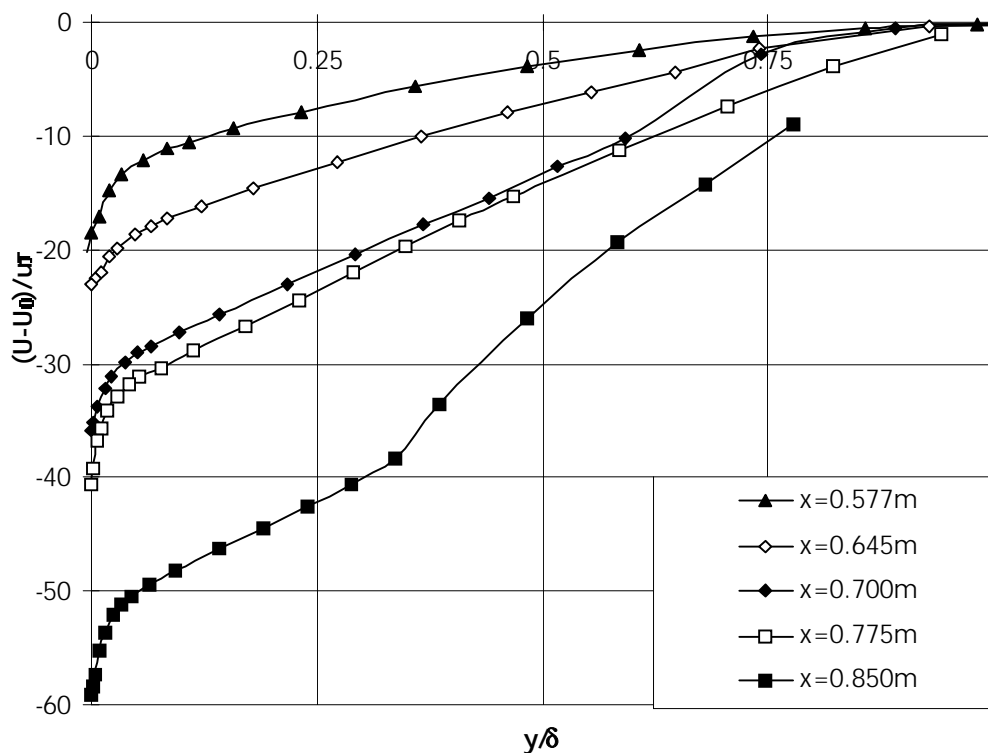

Figure 30. Velocity profiles in case 3 plotted in Clauser scaling.

5.2. Perry-Schofield co-ordinates

Perry and Schofield [19] suggested a scaling using two parameters, the length scale B and the velocity scale u_s. The idea is that the mean velocity profiles in an adverse pressure gradient flow should collapse onto a single function f when scaled with these parameters according to

$$\frac{U_\infty - U}{u_s} = f(\frac{y}{B})$$

- 39 -

The length scale B, which is a kind of boundary layer thickness, is given by Perry and Schofield as B= $2.86\delta^*U_\infty/u_s$. Dengel and Fernholz [9] have approximated the non-dimensionalised velocity profile f with a 7th order polynomial:

$$f(\zeta)=0.781 - 0.535\zeta -0.739\zeta^2 - 2.352\zeta^3 + 13.81\zeta^4 - 33.178\zeta^5 + 36.502\zeta^6 -14.324\zeta^7,$$

where $\zeta=y/B$. [Note that the sign of the constant before ζ^6 should be a plus and not a minus as typed in [9]] The velocity scale u_s can be chosen in several ways - Perry and Schofield related it to the maximum Reynolds shear stress in the profile, Dengel and Fernholz found an approximate correlation

$$\frac{u_s}{U_\infty} \approx 1.01+ 0.485\chi_w$$

relating it to the back-flow coefficient and it may also be chosen to give the optimum fit between the measured velocity profile and the Perry-Schofield profile. The latter approach is the one that has been chosen in the present investigation. According to Dengel and Fernholz, Perry-Schofield scaling works close to separation, where 2.2<H<3.2, for the central part of the boundary layer, 0.025<y/B<0.92.

Only at the most down-stream position in case 3, the shape factor H of the velocity profile was large enough to allow the Perry-Schofield co-ordinates to be used accurately according to [1]. In figure 31 below, the profile suggested by Dengel and Fernholz (DF3.5) [9] has been plotted along with the profile measured with hot-wire at x=0.85 m in case 3. The velocity scaling u_s has been chosen to 29 m/s for a maximum fit with DF's profile. The agreement is acceptable considering that H is near the end of the range of validity for the Perry-Schofield scaling. Using the original P-S gives a less unsatisfactory fit.
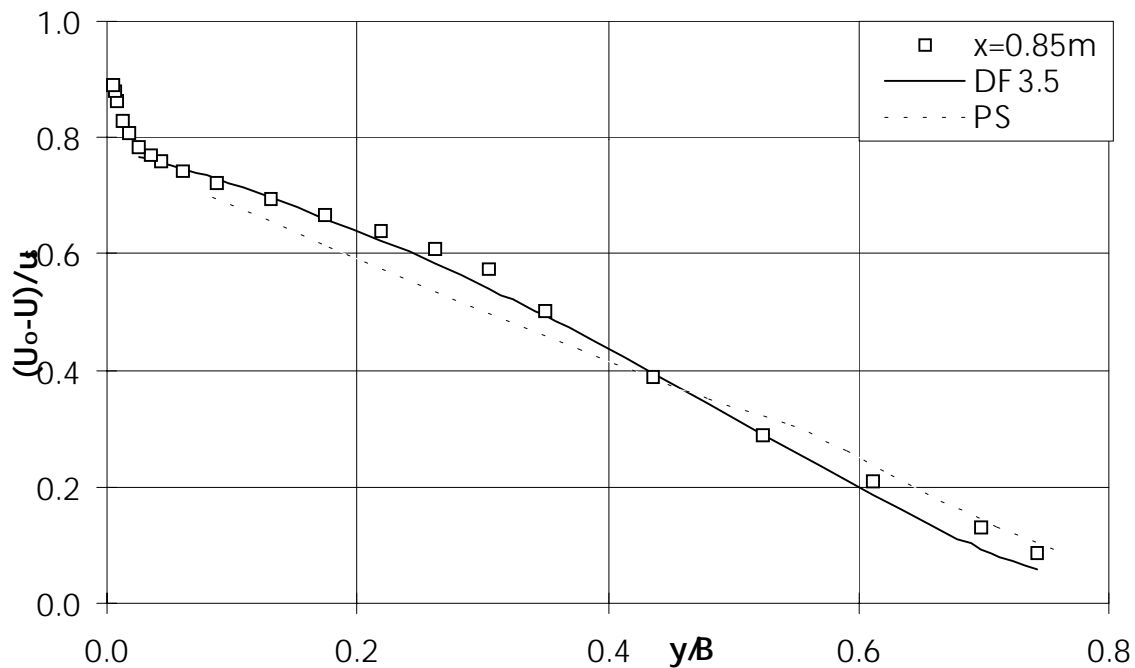

Figure 31. The velocity profile in Perry-Schofield scaling at the x=0.85 m position in case 3, where H=2.42, compared to the original P-S profile (PS) and the profile suggested by Dengel and Fernholz (DF3.5).

5.3. Coles' wall-wake profile

Coles [8] suggested that the standard zero pressure gradient profile of a turbulent boundary layer with a linear and a logarithmic sub-layer could be modified through the addition of a wake function that comes into effect gradually as the outer edge of the boundary layer is approached:

$$\frac{U}{u_\tau} = f(\frac{u_\tau y}{\upsilon}) + \frac{\Pi(x)}{\kappa} w(\frac{y}{\delta})$$

In this relation $f(y^+)$, is the standard logarithmic profile, $f(y^+) = \kappa^{-1} \ln y^+ + B$, which is valid for $y^+ > 30$ ($\kappa \approx 0.41$ is Kàrmàn's constant and $B \approx 4.9$ is the logarithmic intercept). The wake function $w(y/\delta)$ describes how the wake modification comes into effect with increasing y – here it has been fitted to the data given by Coles (see table 1 in [8]):

$$w(\frac{y}{\delta}) = 2\sin^2 \frac{\pi y}{2\delta}$$

Π may vary with x and describes how retarded the boundary layer is and how well-developed the wake region is. Coles gives

$$\Pi(x) = \kappa \frac{\delta^* U_\infty}{\delta u_\tau} - 1$$

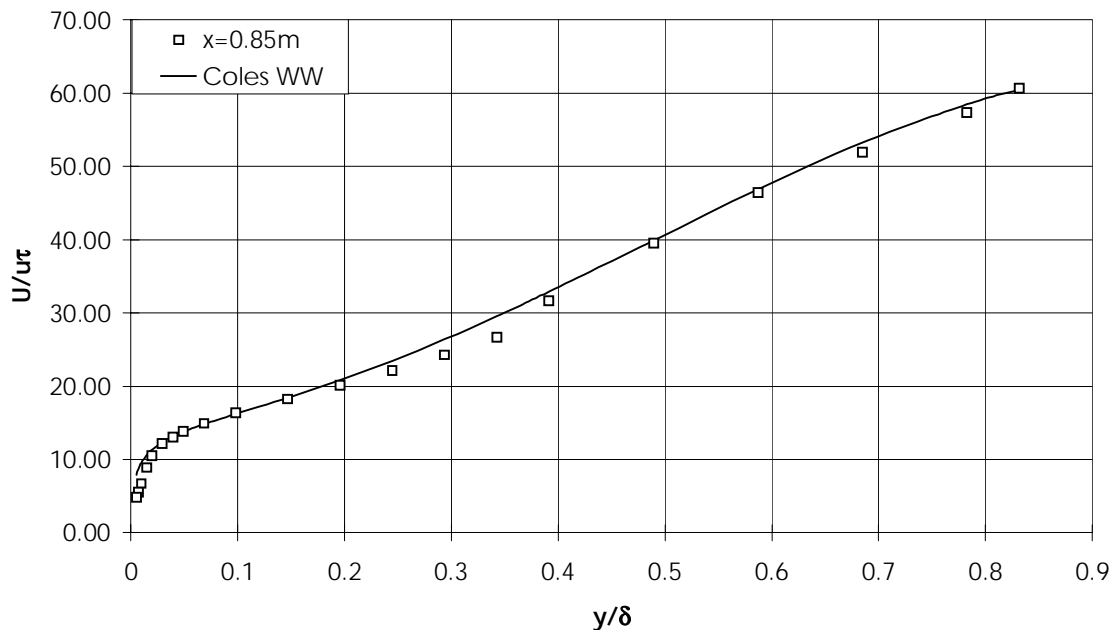When using the values at x=0.85 m in case 3, this gives the below profile.

Figure 32. The profile obtained in case 3 at x=0.85 m using hot-wire, compared to the profile given by Coles wall wake law with u_τ and δ chosen to get an optimum fit.

Figure 32 shows the match between the measured and calculated profiles, when u_τ and δ are chosen so that as good a match as possible is acquired. u_τ=0.41 m/s and δ=23 mm, which is close to the values found in a Clauser plot u_τ=0.46 m/s and from PIV data at x=0.85 m, δ=22 mm.

6. Separation prediction

In many practical applications, it is essential to be able to predict the position of flow separation, since it has a great effect on performance and heat transfer. Unfortunately, it has proven rather difficult to predict where a turbulent boundary layer separates. As Dengel and Fernholz (DF) [9] have shown, even a few per cent variation of the pressure gradient in a strongly decelerated flow may be enough to trigger mean flow separation and cause large changes in the flow structure.

One separation criterion that is often used, is that the shape factor H should reach a certain value at separation and then decrease to this value again at reattachment. This is based on the assumption that turbulent velocity profiles according to Schlichting [24] can be described approximately as a one-parameter family of curves where the velocity profile where $\partial u/\partial y=0$ at the surface is just one of these curves. The DF experiments confirm that there is such a family of profiles, the Perry-Schofield profiles, but only relatively close to separation. The dynamical similarity is also limited to the centre portion of the boundary layer and does not include the near-wall region where separation first occurs. Much effort has been spent on finding the critical value of the shape factor H at separation and reattachment. Unfortunately, no universal critical value of H has been found; Schubauer and Spangenberg's [25] experiment gave values of H in the 2.1-2.4 range, while the separation bubble experiments by AF [1] suggested H=2.85 at separation and reattachment. Other experiments have provided examples of H reaching even higher values, e g 4.00-4.05 according to Rotta [22] before separation. DF [9] suggest that the highest values of H at separation are the result of the back-flow coefficient being measured too far out from the wall. This gives a too low value of the wall back-flow coefficient and makes it seem like the separation point is farther downstream than it actually is, thereby giving a too high value of H at separation. Earlier researchers, including Coles and Rotta, had applied Coles' law of the wake to velocity profiles close to separation, where the profiles actually diverge from that law. According to DF [9], this meant that they also arrived at an erroneous theoretical value of H at separation. Kline, Bardina and Strawn [15] propagate the opposite standpoint, suggesting that mean reattachment occurs at H=4.0 and that the lower shape factor found in certain experiments is a result of the measurement techniques used actually giving the position of incipient separation ($5<\chi_w<20\%$) rather than of mean separation. The earlier quoted experiment of Schubauer and Spangenberg is an example of such an investigation. Early numerical simulations are in error because they, according to Kline et al, either use turbulence models that are not sophisticated enough to capture the changing nature of turbulence once incipient detachment is reached, or mistake the point where the boundary layer integral equations become singular for the position where the wall shear stress reaches zero. Sajben and Liao [23], who examined different scaling laws, found that the difference in H at separation predicted by Coles' wake law and the Perry-Schofield scaling is small – both give values of around H=2.7 at intermittent transitory detachment, $\chi_w=20\%$. DF's experiments just like AF's suggested a value of H=2.85 at mean separation ($\chi_w=50\%$) under the circumstances of that experiment, but according to DF, a different value of H may appear in experiments where the level of free-stream turbulence, Reynolds number or bubble size is different. In the present experiment H was not measured at separation, but at mean reattachment it was found to be 3.1-3.4.

DF found that not only did $\chi_w=0.5$, H=2.85 and $\tau_w=0$ Pa coincide in the case that they studied; H also varied approximately linearly with χ_w, $H\approx2.2+1.4\chi_w$, at least for $\chi_w<0.8$

(according to figure 7 in [9]). A similar correlation, but with a much stronger dependence on the back-flow coefficient, can be found using Kline et al's data; figure 7 in [15] suggests $H \approx 2.15 + 3.70\chi_w$, even though the spread in data is considerable. A more extensive, albeit somewhat dated, discussion about separation and shape factors can be found in Schlichting [24]. Given the great variation of H at separation obtained in earlier studies, it remains questionable whether there is a one-parameter family of curves describing the profiles close to separation and hence a certain value of H that is always obtained at separation.

For a more in-depth discussion of separation criteria and their similarities, is referred to Sajben and Liao's article [23]. Arguing that detachment occurs when what they refer to as the normalised specific momentum defect as a function of the form factor has a maximum, they show that a number of separation criteria based on one parameter curve families - Coles wake law, Perry-Schofield co-ordinates and the entrainment formulae by Head and Green are very similar. The normalised specific momentum defect is defined as $\theta/(\delta_{0.995} - \delta^*)$, i e the ratio between the momentum defect per unit mass caused by the presence of the boundary layer and the momentum per unit mass in the free-stream. Agreement with experimental data by Simpson et al, was a little less impressive, but still satisfactory. Sajben and Liao also argue that what Simpson [26] refers to as intermittent transitory detachment (ITD), i e $\chi_w = 0.2$, is really what should be compared to complete laminar separation, instead of transitory detachment, $\chi_w = 0.5$, due to the profound effects on the flow ITD has.

An earlier attempt at simulating the growth of boundary layers was performed by Rotta [22]. In that investigation, a method based on integral momentum and energy integrals together with empirical formulae for wall shear stress and energy dissipation coefficients were used. Rotta showed that deviations from two-dimensionality in the flow had to be taken into account, if not the tendency towards separation was to be underestimated. The study also showed that while the agreement with measured Re_θ was relatively satisfactory in many cases, the shape factor H and the skin friction coefficient C_f deviated significantly from experimental results, especially close to separation.

Accurate predictions of the position of the separation line can be made, provided that the displacement thickness $\delta^*(x)$ is considered a known variable, according to DF [9]. Since this is normally not true at the design stage, before an experimental evaluation of a geometry has been performed, one has to resort to integral methods, e g the Twaites and Kàrmàn-Pohlhausen methods for laminar boundary layers, to simulate the development of the boundary layer. The latter method has also been modified by Buri [5] so that it can be applied to turbulent boundary layers. These methods take the local pressure gradient as well as the history of the flow into account and calculate the boundary layer growth. In this examination, Buri's method, which is presented by Schlichting [24], has been used and compared with the results from calculations using Stratford's criterion, the method presented by Duncan et al [10] and the experimental results.

In all the following methods, the measured pressure distribution was used in case 3, while a pressure distribution deduced from the flow velocity at the inlet and the geometry of the bump was used in case 1a. The reason for this is that the static pressure as measured at the plate tends to remain constant in the horizontal direction in the separated region, even though the main flow is strongly expanded there. This should make the prediction of separation clearer and demonstrate the ability of the methods to correctly predict separation based solely on parameters available at the design stage. This approach has the drawback that it neglects

the influences of a. the growing boundary layers, which give a higher free-stream velocity and b. the suction which removes fluid through the ceiling and lowers the free-stream velocity. Hopefully, these tendencies will cancel out one another.

6.1. Stratford's method

In his article from 1959 [30], Stratford suggested that

$$C_P \sqrt{(x \frac{dC_P}{dx})} = 0.39 \sqrt[10]{(10^{-6} \, \text{Re}_x)} \quad (6.1.1)$$

at separation when $C_p \leq 4/7$ and $d^2p/dx^2 \leq 0$. For $d^2p/dx^2 > 0$, the numerical coefficient 0.39 in the right hand side of the above relation should be replaced with 0.35.
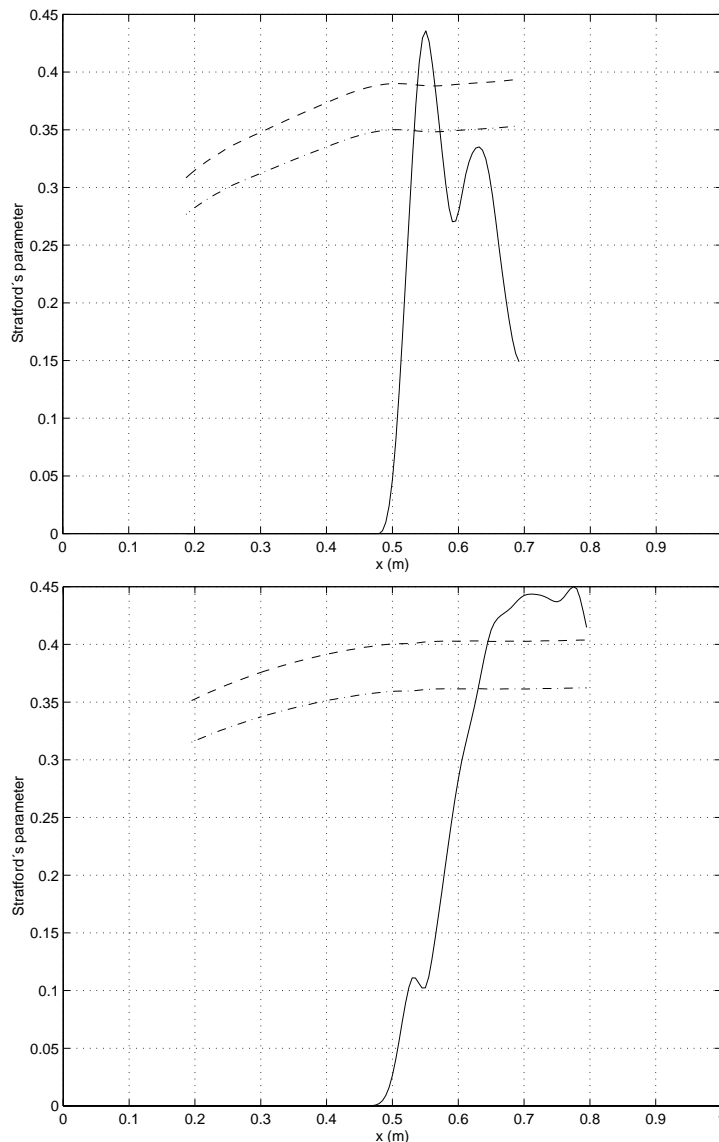
Figure 33a and b. The separation criterion due to Stratford – the left hand side (solid line) and right hand side (dashed and dash-dotted lines corresponding to the 0.39 and 0.35 coefficients, respectively) of equation 6.1.1 for case 1a and case 3.

Figure 33 shows the results of applying the Stratford criterion in two of the flow cases examined here. The measured static pressures were used in calculating the C_p's. In case 1a, separation was predicted to occur as early as at x=0.54 m, while it was not observed until at

x=0.65 m. The method also failed in case 3, where it predicted separation at x=0.64 m, whereas no separation at all was found experimentally in that case.

The second peak seen in figure 33a indicates that the method may be modified so that the first peak falls below the threshold indicating separation, leaving the second peak in place to give an acceptable prediction of the separation position. This would be accomplished if more weight were put on C_P and less on dC_P/dx in Stratford's formula.

6.2. Buri's method

In laminar boundary layers, Twaites' criterion that $Re_\theta^2 K=-0.082$ (or frequently -0.09) at separation can be used. In turbulent boundary layers, the scaled pressure gradient gamma, $\Gamma=\theta/U \ dU/dx \ Re_\theta^{0.268}$ is used in the method proposed by Buri, which is presented by Schlichting [24]. Separation is according to Schlichting found close to $\Gamma=-0.06$. Buri's method predicts the momentum thickness growth as:

$$\frac{d}{dx}(\theta \cdot Re_\theta^{0.268}) = 0.016 - 4.05\Gamma$$

The constants that have been selected above are somewhere in the middle of the ranges given in Schlichting (0.01475-0.0175 and 3.94-4.15) – in reality they vary somewhat with H, especially close to separation. The early laminar part of the boundary layer was handled separately; here an approximate Kàrmàn-Pohlhausen method with H=2.55 was used. Buri's method is quite robust against slight errors in the initial θ of the turbulent boundary layer, so the exact position of the transition, here x=0.18 m, and the laminar boundary-layer growth are of little significance.
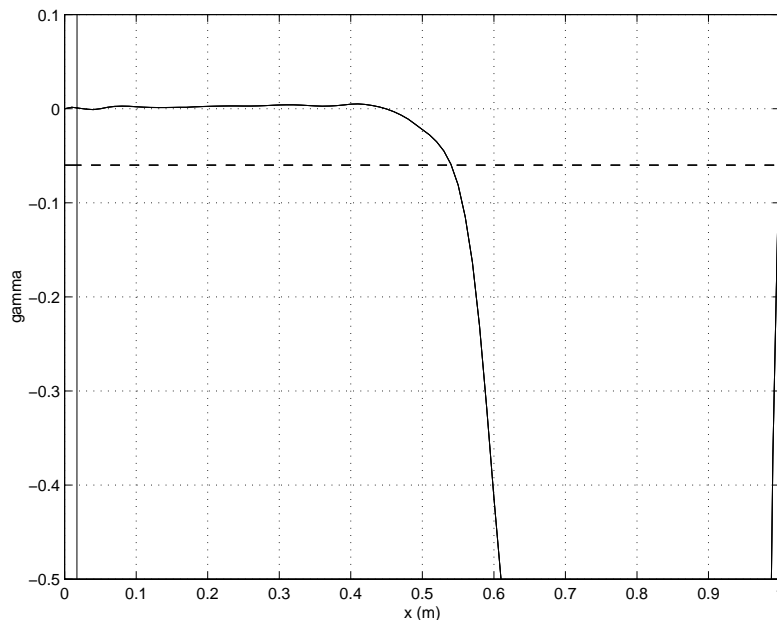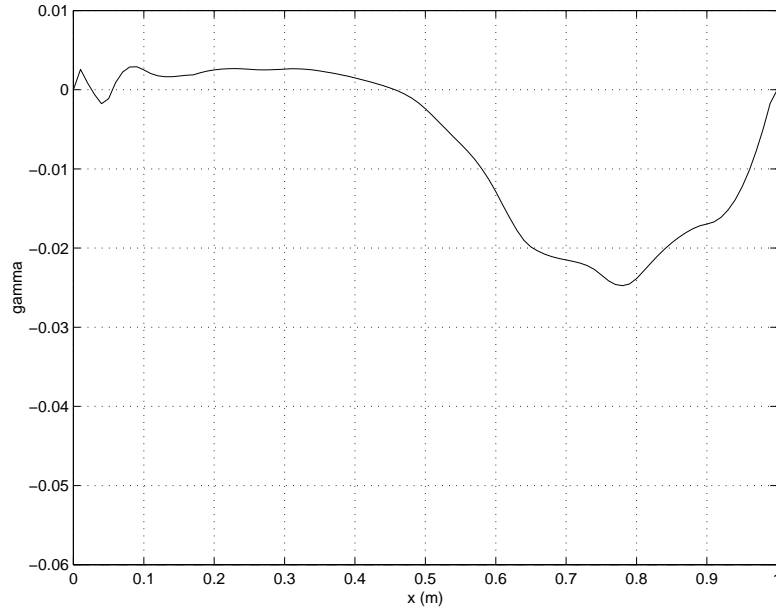
Figure 34a and b. The development of the shape factor Γ in case 1a and case 3 as calculated using Buri's method.

As is shown in figure 34 above, this method fails to predict the position of separation in case 1a, indicating separation at around x=0.53 m. This seems to coincide more closely with the position where the static pressure curve departs from the curve suggested by the geometry due to intermittent separation, than with the position of mean separation. In case 3, no separation is predicted to occur.

Re-examining the constants chosen in the right hand side reveals that this combination of constants gives the wrong boundary-layer development at ZPG as well as a very low value of H at separation (approximately 1.6). A more reasonable choice of constants from this perspective would be 0.020 and 5.93, respectively. Unfortunately, these constants give values of H during the deceleration that are far below those found experimentally, so in summary, a more complex method is needed to predict the development of a boundary layers subjected to different pressure gradients. Comparison of Γ and H vales found experimentally indicates that no straightforward relationship between these variables exists, which is one assumption on which Buri's method rests. On the other hand, the prediction of the boundary layer thickness growth, which is shown in figure 35, is impressive, considering that the only input data required is the free-stream velocity development in the down-stream direction.

6.3. Duncan et al's method

A third method that was tested, used the integral momentum equation:

$$\frac{d\theta}{dx} + (2+H)\frac{\theta}{U_\infty}\frac{dU_\infty}{dx} = \frac{\tau_w}{\rho U_\infty^2}$$

where H is calculated using the formula suggested by Duncan, Thom and Young [10]:

$$\frac{1}{U_\infty}\frac{d}{dx}(U_\infty\theta\frac{2H}{H-1}) = F(H)$$

- 46 -

Assuming that the velocity profiles are given by a power law with an exponent that varies in the down-stream direction, the right hand side of this equation is equal to the x-derivative of the mass flux. F is a function of H which is chosen to fit experimental data to F(H)=*const*·(H-1.1). A survey of experimental data from different investigations showed considerable scatter when plotted in an F-H diagram, so the constant may be assigned any value in the 0.01 – 0.06 range. The initial boundary layer thickness and the constant dF/dH were chosen so that a good correlation between simulations and experiments was attained in case 3.

As a third relation that is necessary to extract all three unknowns – τ_w, θ and H – the following empirical relation was used, based on the data in DF [9]:

$$\tau_w = 1.2\rho U_\infty^2 \, Re_\theta^{-0.268} \cdot 10^{1.5H}$$

These relations lead to the boundary layer development found in figures 35-37. In figure 35, the momentum thickness growth predicted by the methods by Buri and Duncan are plotted. As for the other methods presented here, the results are only valid up to separation in case 1a.
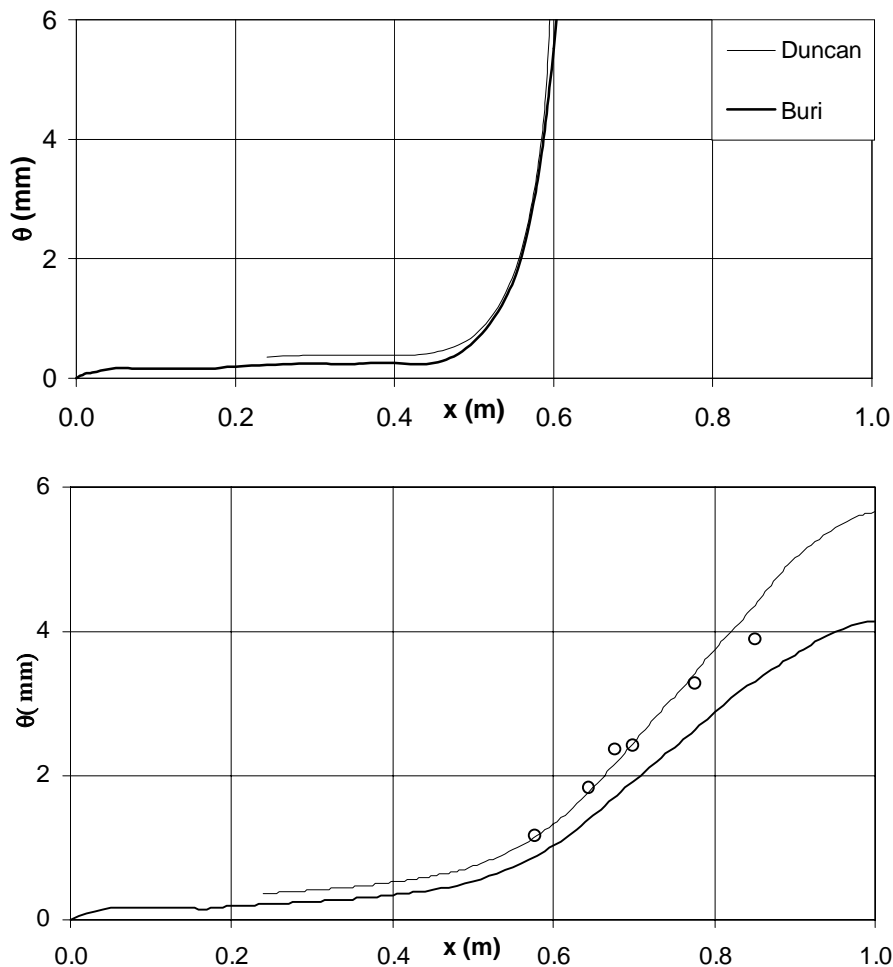

Figure 35a and b. The momentum thickness in case 1a (throat velocity 39.5 m/s) and case 3 (throat velocity 39.0 m/s) as computed using the methods proposed by Buri and Duncan et al. In the latter case, the momentum thickness found experimentally has also been plotted.
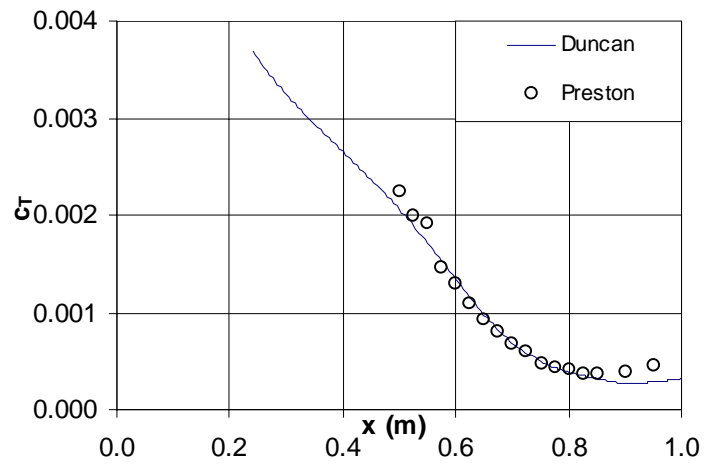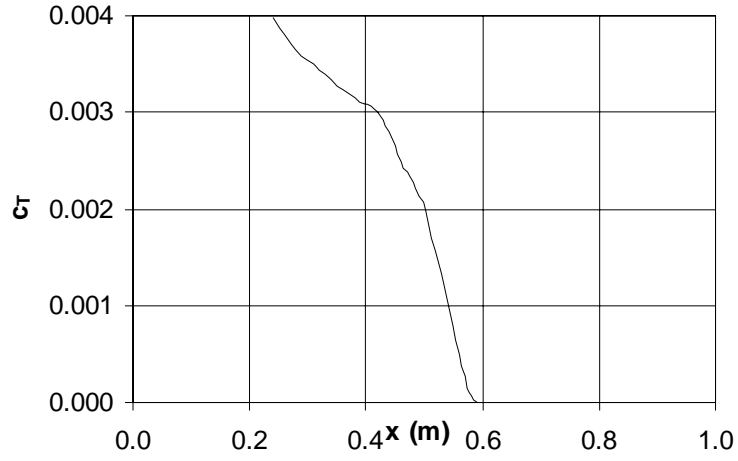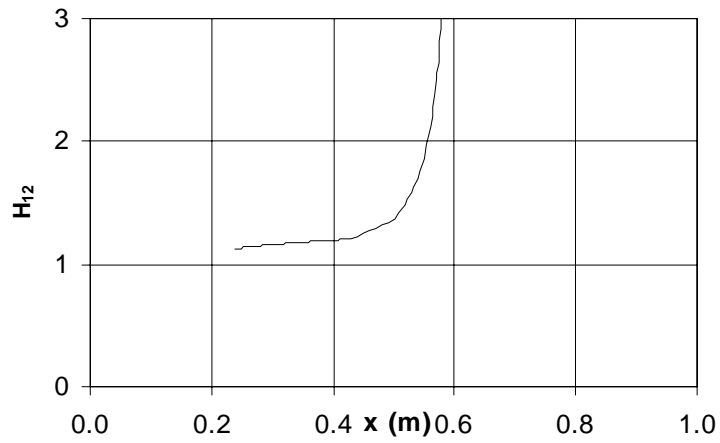
Figure 36a and b. Wall shear stress coefficient $c_T=\tau_w/(\rho U^2)$ calculated using the method proposed by Duncan et al [10] in cases 1a and 3, compared to measurements using Preston tubes.
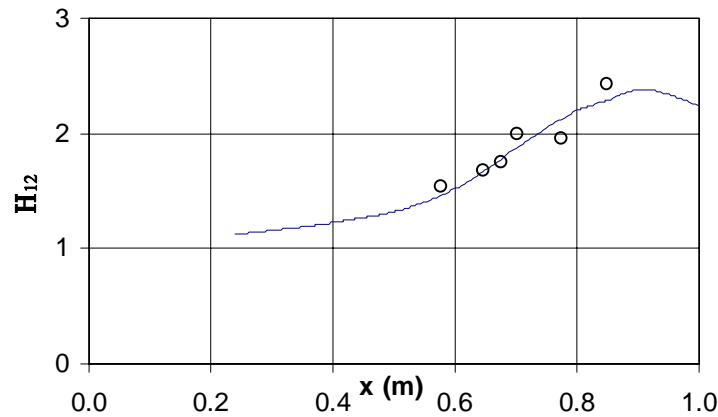
Figure 37a and b. The shape factor H as given by the method of Duncan et al in case 1a and 3. In the latter case, they are compared to shape factors attained from hot-wire velocity profiles.

Figure 37b shows that very good agreement is reached between the calculated and measured shape factors H in case 3. While the method correctly predicts that no separation occurs in this case, it suggests that separation occurs at x=0.58 m in case 1a, where the wall shear stress is zero and the shape factor H rises rapidly above 3.3. The separation is thus predicted to occur some distance up-stream of the x=0.65 m found experimentally.

6.4. Summary

In summary one can note that all three of the tested methods seem to be over-sensitive to the strong adverse pressure gradients applied here, under-predicting the ability of the boundary layer to withstand these gradients for some distance before separating. Of the three methods, Stratford's criterion is the one that is simplest to apply but the least successful one. The methods suggested by Buri and Duncan et al are far more accurate, but require more calculations since they involve integration in the x-direction. Of these two methods, Duncan's is the most accurate, but it requires some knowledge of the growth of the boundary layer to give accurate predictions of the point of separation.

7. Conclusions

In the present investigation, APG flows both with and without separation have been studied. Despite the fundamentally different nature of the flows, the pressure recoveries attained over the plate all fall in the 0.47 - 0.62 range. The highest pressure recoveries are achieved in the least rapidly expanded flow (cases 2 and 3) and towards the end of the plate for this expansion, the same C_p is attained both with and without separation on the plate. This suggests that separation occured in the ceiling instead of on the plate in case 3.

In the attached flow case studied here, Preston tube measurements and Clauser plots of the mean velocity profile still give fair values for the wall shear stress, despite the fact that p^+ is quite high. At the most down-stream position p^+=0.05 and as can be seen in figure 20, there is still a logarithmic layer in the boundary layer, even though it does not stretch as far out as the logarithmic layer at more upstream positions. This means that it should be possible to find calibration functions valid for Preston tubes of a certain size even close to separation. At least, it can be concluded that p^+ is not a good parameter to tell whether or not there is a logarithmic layer.

The perturbation velocity moments of the streamwise velocity are found to change during the APG so that the near-wall peak in u_{rms} is gradually replaced by a smoother peak further out at around 0.45δ, as the shape factor H increases above 1.8. On the other hand, a sharp near-wall peak develops in the skewness and flatness of the streamwise velocity u as separation is approached. While the boundary layer development qualitatively follows that of earlier experiments and simulations, there is a great deal of quantitative differences, suggesting that conventional inner and outer scales are not that useful in adverse pressure gradients, even when comparing profiles with the same H obtained in different investigations. There seem to be more parameters that control the development of boundary layers subjected to APG.

H at reattachment seems to be in the 3.1-3.4 range rather than 2.85 as found in AF's experiment [1]. Due to the low resolution of PIV measurements, the flow closest to the plate cannot be examined and the precision in the determination of H at reattachment is low. While θ increases monotonically over the separation bubble and the reattachment region, δ^* actually declines near the reattachment.

The separation prediction criterion given by Stratford grossly under-predicts the ability of a turbulent boundary layer to withstand the strong adverse pressure gradients of the present experiment. Momentum integral methods give better predictions, even though they also indicate separation too early in the strongly decelerated case 1a. While Buri's method only needs the geometry and inlet flow velocity of the configuration under test, Duncan's method requires that the boundary layer thickness is known from experiments and can be used to adjust the empirical parameters of the method.

PIV provides a non-intrusive technique for analysing flows in separated flow fields with a fair degree of accuracy and resolution. To achieve this, the smoke density and the light intensity must be high and the pictures taken must be properly defocused, or else the velocities measured tend to be discretised by the pixel size of the PIV picture pair. To get smoke to fill the separated region does not seem to be a major problem. On the other hand, to get smoke particles so far out that the free-stream velocity can be determined accurately seems to be troublesome. When it comes to resolution in time, space and velocities,

conventional hot-wire measurements are superior to PIV results. In order to get reasonably good mean velocity fields from PIV data in the present case, at least 300 picture pairs seem to be needed. If u_{rms} is to be calculated as well, an even larger number of picture pairs is needed.

Separated turbulent boundary layers of the studied type tend to be very sensitive to small pressure differences in the spanwise direction and it is very hard to establish a straight separation line perpendicular to the direction of the free-stream without a separation trip. This instability might be due to imperfections in the experimental set-up used that introduce small varying disturbances in the spanwise directions. A higher capacity suction system capable of removing all of the ceiling boundary layer would hopefully make the use of a large separation trip unnecessary. The complex nature of separated turbulent boundary layers means not only that experimental investigations meet with a number of difficulties, but also that separation can be studied from many different perspectives. Further investigations into this phenomenon that has so far-reaching practical implications are much needed.

Acknowledgements

References

1   Alving, A. E., Fernholz, H. H., "Mean-velocity scaling in and around a mild, turbulent separation bubble", *Phys. Fluids* 7 (1995)

2   Alving, A. E., Fernholz, H. H., "Turbulence measurements around a mild separation bubble and down-stream of reattachment", *Journal of Fluid Mechanics* 322 (1996)

3   Angele, K., private communication

4   Bertelrud, A. *Flow disturbances associated with Preston tubes in turbulent boundary layers*, Report 127 of The Aeronautical Research Institute of Sweden (1977)

5   Buri, A., *Eine Berechnungsgrundlage für die turbulente Grenzschicht bei beschleunigter und verzögerter Strömung*, Diss. Zürich (1931)

6   Chue, S. H., "Pressure probes for fluid measurements", *Prog. Aerospace Sci.* 16 no 2 (1975)

7   Clauser, F. H., "Turbulent boundary layers in adverse pressure gradients", *J. Aero. Sci.* 21 (1954)

8   Coles, D., "The law of the wake in the turbulent boundary layer, *Journal of Fluid Mechanics* 1 (1956)

9   Dengel, P., Fernholz, H. H., "An experimental investigation of an incompressible turbulent boundary layer in the vicinity of separation", *Journal of Fluid Mechanics* 212 (1990)

10   Duncan, Thom & Young, *Mechanics of Fluids*, Edward Arnold Printers Ltd, London (1970)

11   *FLOwareInstallation & User's guide*, Dantec Measurement Technology (1996)

12   Henkes, R. A. W. M., Skote, M., Henningson, D. S., "Application of turbulence models to equilibrium boundary layers under adverse pressure gradient", *TSF* 11 (1997)

13   Hoffmann, J. A., Gonzalez, G., "Effects of small scale, high intensity turbulence on flow in a two-dimensional diffuser", *Journal of Fluids Engineering* 106 (1984)

14   Keane, R. D., Adrian, R. J., "Theory of cross-correlation analysis of PIV images", *Applied Scientific Research* 3 (1992)

15   Kline, S. J., Bardina, J. G., Strawn, R. C., "Correlation of the Detachment of Two-Dimensional Turbulent Boundary Layers", *AIAA Journal* 1 (1993)

16   Mayle, R. E., "The Role of Laminar-Turbulent Transition in Gas Turbine Engines", *Transactions of the ASME (Journal of Fluids Engineering)* (1991)

17   Na, Y., Moin, P., "Chapter 5 - *Separated turbulent boundary layer", Direct numerical simulation of turbulent boundary layers with adverse pressure gradient and separation Report No TF-68* (1996), Termosciences Division, Department of Mechanical Engineering, Stanford University, (1996)

18   Nikuradse, J. "Untersuchungen der die Strömungen des Wassers in konvergenten und divergenten Kanalen", *Forsch. -Arb. Geb. Ing. -Wes. 289* (1929)

19   Perry, A. E., Schofield, W. H., "Mean velocity and shear stress distributions in turbulent boundary layers", *Physics of Fluids* Dec (1973)

20   Rao, D. M., Kariya, T. T., "Boundary-layer submerged vortex generators for separation control - an exploratory study", AIAA 88-3546-CP 2 (1988)

21   Rotta, J., "Beitrag zur Berechnung der turbulenten Grenzschichten", *Ingenieur-Archiv* 19 (1951)

22   Rotta, J., "Vergleichende Berechnungen von turbulenten Grenzschichten mit verschiedenen Dissipationsgetetzen", *Ingenieur-Archiv* 38 (1969)

23   Sajben, M., Liao, Y., "Criterion for the Detachment of Laminar and Turbulent Boundary Layers", *AIAA Journal* 11 (1995)

24   Schubauer, G. B. and Spangenberg, W. G., "Forced mixing in boundary layers", *Journal of Fluid Mechanics* 8: 10-32 (1960)

25   Schlichting, H., *Boundary-Layer Theory*, 7th Ed. McGraw-Hill, New York (1979)

26   Simpson, R. L., "Turbulent boundary-layer separation", *Annual Review of Fluid Mechanics* 21 (1989)

27   Skåre, P. E., Krogstad, P-Å, "A turbulent equilibrium boundary layer near separation", *Journal of Fluid Mechanics* 272 (1994)

28   Spalart, P. R., Coleman, G. N., "Numerical study of heat transfer in a separation bubble", *European Journal of Mechanics - B/Fluids* 2 (1997)

29   Stratford, B. S., "An experimental flow with zero skin friction throughout its region of pressure rise", *Journal of Fluid Mechanics* 5 (1959)

30   Stratford, B. S., "The prediction of separation of the turbulent boundary layer", *Journal of Fluid Mechanics* 5 (1959)

31   Tennekes, H., Lumley, J. L., *A First Course in Turbulence*, MIT press, Cambridge (1972)

32   Yaglom, A. M., "Similarity laws for constant-pressure and pressure gradient turbulent wall flows", *Annual Review of Fluid Mechanics* 11 505 (1979)